



**HAL**  
open science

# Timing and duration of Archean orogenic gold deposits in the Bourlamaque pluton, Val d'Or mining camp, Abitibi, Canada

Alain Tremblay, Gilles Ruffet, Jérémie Lemarchand

## ► To cite this version:

Alain Tremblay, Gilles Ruffet, Jérémie Lemarchand. Timing and duration of Archean orogenic gold deposits in the Bourlamaque pluton, Val d'Or mining camp, Abitibi, Canada. *Ore Geology Reviews*, 2020, 127, pp.103812. 10.1016/j.oregeorev.2020.103812 . insu-02957471

**HAL Id: insu-02957471**

**<https://insu.hal.science/insu-02957471>**

Submitted on 5 Oct 2020

**HAL** is a multi-disciplinary open access archive for the deposit and dissemination of scientific research documents, whether they are published or not. The documents may come from teaching and research institutions in France or abroad, or from public or private research centers.

L'archive ouverte pluridisciplinaire **HAL**, est destinée au dépôt et à la diffusion de documents scientifiques de niveau recherche, publiés ou non, émanant des établissements d'enseignement et de recherche français ou étrangers, des laboratoires publics ou privés.

## Journal Pre-proofs

Timing and duration of Archean orogenic gold deposits in the Bourlamaque pluton, Val d'Or mining camp, Abitibi, Canada

Alain Tremblay, Gilles Ruffet, Jérémie Lemarchand

PII: S0169-1368(20)30709-5

DOI: <https://doi.org/10.1016/j.oregeorev.2020.103812>

Reference: OREGEO 103812

To appear in: *Ore Geology Reviews*

Received Date: 3 July 2020

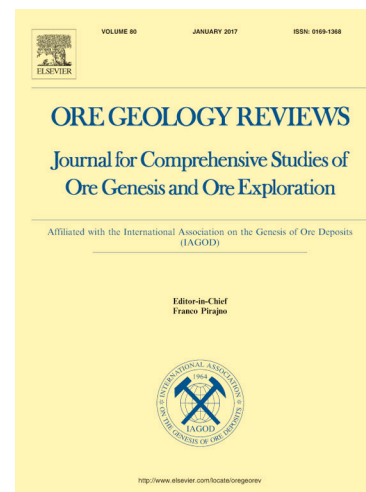
Revised Date: 24 September 2020

Accepted Date: 28 September 2020

Please cite this article as: A. Tremblay, G. Ruffet, J. Lemarchand, Timing and duration of Archean orogenic gold deposits in the Bourlamaque pluton, Val d'Or mining camp, Abitibi, Canada, *Ore Geology Reviews* (2020), doi: <https://doi.org/10.1016/j.oregeorev.2020.103812>

This is a PDF file of an article that has undergone enhancements after acceptance, such as the addition of a cover page and metadata, and formatting for readability, but it is not yet the definitive version of record. This version will undergo additional copyediting, typesetting and review before it is published in its final form, but we are providing this version to give early visibility of the article. Please note that, during the production process, errors may be discovered which could affect the content, and all legal disclaimers that apply to the journal pertain.

© 2020 Published by Elsevier B.V.





38 preserve evidences for at least two subsequent disturbances linked to probable  
39 hydrothermal circulation events at c. 2667 Ma and c. 2652 Ma. White micas  $^{40}\text{Ar}/^{39}\text{Ar}$   
40 age spectra from auriferous quartz veins and hosting mylonitic shear zones are typical of  
41 long-lasting and sequential dynamic recrystallization and suggest that Au-bearing  
42 hydrothermal circulation was establish, at least, around c. 2650 Ma, and followed by a  
43 succession of hydrothermal pulses at c. 2597, 2575, 2551, 2500 and 2452 Ma.  $^{40}\text{Ar}/^{39}\text{Ar}$   
44 ages distribution among the different deposits as well as between the auriferous quartz  
45 veins and hosting shear zones are consistent with fluids production and circulation along  
46 an active network of seismically active fault zones.

47 Keywords: Superior Province, Abitibi, orogenic gold, geochronology, duration.

48

## 49 **1. Introduction**

50 Orogenic gold deposits (Groves et al., 1998) are a widespread type of epigenetic  
51 ore deposits attributed to faulting and fracturing of the lithosphere and coeval  
52 hydrothermal fluid circulation at/or in the vicinity of compressional/transpressional plate  
53 boundaries. These gold deposits occur in accretionary terranes and collision zones of all  
54 geological periods but those hosted by Late Archean rocks worldwide contain a high  
55 percentage of the world gold resource (Goldfarb et al., 2001). Active crustal deformation  
56 is necessary to generate and maintain permeability and to sustain large-scale fluid flow in  
57 such hydrothermal systems (Cox, 2005), and isotopic geochronological data suggest that  
58 major deposits of a given mining district formed diachronically towards the end of c. 100  
59 to 200 m.y. long evolutionary history of hosting rocks (e.g. Groves et al., 2000). In the  
60 Val d'Or mining district, most veins-type orogenic gold deposits, typified by the Sigma-  
61 Lamaque deposit (Daigneault, 1983; Robert and Brown, 1986; Dubé, 2018), have been  
62 interpreted either as shear zone-hosted (Sibson et al., 1988; Dubé, 2018) or fold-  
63 controlled (Cowan, 2020). In the Sibson's et al. (1988) fault-valve model of crustal-scale  
64 shearing, for instance, fluid pressure ( $P_f$ ) build-ups below the seismogenic zone are linked  
65 with episodic seismic failures of the crust, the up-dip propagation of reverse fault-  
66 fractures and the drainage of mineralizing fluids along faults and related zones of fracture  
67 permeability, followed by post-failure mineral deposition and self-sealing (see also

68 Robert and Poulsen, 2001; Sibson, 2001; and Cox, 2001; 2005). That model has been,  
69 however, recently re-evaluated and disputed for the Sigma-Lamaque deposit (Cowan,  
70 2020) but it still adequately accounts for gold-vein deposits hosted by isotropic  
71 batholithic intrusions such the Bourlamaque pluton (e.g. Tessier, 1990; Sauvé et al.,  
72 1993; Tremblay, 2001). In terms of  $P_f$  and strain rate ( $\dot{\gamma}$ ) (Fig. 1), the lifespan of such  
73 hydrothermal systems is believe to be concomitant with an unknown number of seismic  
74 failure events initiated along neo-formed and pre-existing reverse faults at the base, more  
75 or less, of the seismogenic zone, their functioning being synchronous with inter-seismic  
76 episodes of progressive  $P_f$  increases in excess of the lithostatic load ( $P_f > \Phi_3$ ) lasting from  
77 decades to many thousands of years (Sibson et al., 1988; Sibson, 2001; Cox, 2001; 2005,  
78 among others).

79 In typical vein-type deposits, such as those of the Southern Abitibi Greenstone  
80 Belt of the Archean Superior Province of Canada (Fig. 2), the total reverse separation  
81 across the faults and shear zones hosting the gold mineralization is relatively low, in the  
82 order of a few hundred metres, although the vein systems can be of considerable vertical  
83 extent ( $>2$  km). It has been suggested that this may represent an approximate total  
84 amount of c.  $10^2$ - $10^3$  episodes of  $\sim M7$  seismic failures, if not more, for a single gold  
85 deposit along a given fault/shear zone system (Sibson et al., 1988; Cox, 2005). For  
86 comparison, the total fluid flux volume through mineralized faults of the Eastern  
87 Goldfield Province (Western Australia) suggests that it is the result of many hundreds or  
88 thousands of fault slip events (Sheldon and Ord, 2005). The determination of magnitude-  
89 frequency distributions for large earthquakes is a difficult task. It is highly imprecise,  
90 even in modern tectonic settings (e.g. Berryman et al. 2012; Scharer et al. 2014).  
91 Establishing the age of formation of gold mineralization and the time-period that  
92 corresponds to the development of a given series of fault-controlled auriferous veins is,  
93 however, of considerable importance for exploration and field-based strategies. In  
94 fossilized Archean hydrothermal systems that are accessible via surface exposure and  
95 underground mining, this can be studied by the isotopic dating of appropriate rock units  
96 and structures. Using the  $^{40}\text{Ar}/^{39}\text{Ar}$  dating method and the compilation of U-Pb or Pb-Pb  
97 dating of ore-related minerals, this contribution presents an extensive geochronological

98 study on the timing and the inferred duration of the formation of typical vein-type gold  
99 deposits hosted by the Bourlamaque pluton in the Val d'Or mining district (Fig. 3) of the  
100 Abitibi Greenstone Belt.

101

## 102 **2. Geological setting**

103 The Abitibi Greenstone Belt (AGB) (Fig. 2) is made up of ultramafic, mafic,  
104 felsic volcanic rocks and syn-volcanic intrusions of Late Archean age. The volcanic  
105 domains are separated by narrow and linear belts of clastic sedimentary rocks that are  
106 associated with major fault zones forming lozenge-shaped patterns (Ludden and Hubert,  
107 1986; Hubert, 1990; Percival, 2007). The youngest sequence of these clastic sedimentary  
108 rocks, the Temiskaming Group, was deposited above angular unconformities between ca.  
109 2679 and ca. 2670 Ma (e.g. Robert et al., 2005). Both the volcanic and sedimentary rocks  
110 are intruded by a series of syn- and post-tectonic, dioritic to tonalitic plutons that span  
111 ages as young as ca. 2650 Ma (e.g. Robert, 2001). To the south, the AGB is in fault  
112 contact with the Pontiac subprovince along the Cadillac tectonic zone (CTZ, Fig. 2;  
113 Robert, 1989). The Pontiac subprovince (Figs. 2 and 3) contains rocks that are mainly  
114 younger than c. 2683 Ma (Mortensen and Card, 1993), and which consist of flyschoid  
115 wackes and pelites with minor volcanic rocks intruded by voluminous late tectonic  
116 granitoids (Fig. 2). Regional structures in both the Abitibi and Pontiac subprovinces are  
117 related to north-south compression during the Late Archean Kenoran orogeny (Percival,  
118 2007). Regional metamorphism (~2660 Ma; Robert et al., 2005) is at subgreenschist to  
119 amphibolite facies in the AGB, whereas in the Pontiac subprovince, it increases from the  
120 biotite to the sillimanite zone within c. 2 km south of the CTZ (Dimroth et al., 1983;  
121 Powell et al., 1995).

122 In the Val-d'Or mining district (Fig. 3), rock units strike east-west and are tightly  
123 folded, almost subvertical and parallel to the trend of the regional structural fabric that is  
124 a weak to penetrative schistosity hosting downdip stretching lineations, and which has  
125 been ascribed to a D<sub>2</sub> event of regional deformation (Robert et al., 2005). The youngest  
126 volcanic rocks of the area, the Val d'Or and Héva formations (Fig. 3), yielded U-Pb  
127 zircon ages of  $2704 \pm 2$  and  $2702 \pm 2$  Ma, respectively (Scott et al., 2002). The

128 Bourlamaque pluton ( $2700 \pm 1$  Ma; Wong et al., 1991) is a calc-alkalic synvolcanic  
129 intrusion (Campiglio and Darling, 1976) which hosts several gold deposits (Fig. 3).  
130 Several generations of dikes, predating gold-bearing quartz vein mineralization, occur  
131 throughout the area and include aplite, pegmatite, and, more commonly, diorite dikes, the  
132 latter type has been interpreted as a stress guide for shear zone development in the  
133 Bourlamaque pluton (Belkabir et al., 1993). Syn- to late-tectonic intrusions range from  
134 diorite to tonalite and typically form small plutons that locally host gold-bearing quartz  
135 veins, such as in the Sigma-Lamaque deposit (e.g. Robert & Brown, 1986; Dubé, 2018).  
136 Post-tectonic intrusions consist of quartz-monzonite and granite. The Preissac-Lacorne  
137 batholith (Fig. 2) is a major syn- to late-orogenic intrusion of the Val d'Or mining  
138 district. It is made up of a composite series of intrusions in which two distinct types and  
139 ages of granitic rocks are present: an early, subalkaline to alkaline, monzodiorite-  
140 monzonite-granodiorite-syenite series emplaced between 2690 and 2670 Ma; and a  
141 younger, S-type garnet-muscovite granite series dated between 2660 and 2642 Ma, and  
142 probably derived from a major metasedimentary source (Feng et al. 1992; Ducharme et  
143 al., 1997; Daigneault et al, 2002). Finally, diabase dikes, presumably related to mafic  
144 dike swarms of the latest Archean-Early Paleoproterozoic (2.5-2.45 Ga) Matachewan  
145 Igneous Province (Ciborowski et al., 2015), record the youngest plutonic event of the  
146 area.

147 Robert (1990, 1994) distinguished two types of gold deposits in the Val d'Or  
148 mining district, (1) disseminated gold in massive, fractured, or brecciated wall rocks, and  
149 (2) vein-type orogenic deposits. Within the latter, quartz-carbonate-tourmaline veins are  
150 distinguished from quartz-carbonate-chlorite veins. The timing of the disseminated gold  
151 mineralization (type 1) is constrained by 2692 to 2696 Ma diorite dikes crosscutting the  
152 mineralization (Couture et al., 1994; Morasse, 1998). These deposits are therefore  
153 considered as “early”. By analogy, quartz-carbonate-chlorite veins of type 2 gold deposits  
154 are typically crosscut by mafic dikes, overprinted by deformation, and were also  
155 classified as “old” (Robert, 1994). The auriferous quartz-carbonate-tourmaline veins (i.e.  
156 the quartz-carbonate veins of Robert et al., 2005), classified as “young” by Robert  
157 (1994), were formed after the peak of metamorphism and are almost undeformed. They

158 are hosted by shear zones and quartz-carbonate  $\pm$  tourmaline  $\pm$  scheelite vein systems,  
159 and were typified in the Sigma-Lamaque and the Perron-Beaufor deposits (Fig. 3).  
160 Although that it has been recently contested by Cowan (2020), the formation of gold-  
161 hosting shear zones is usually considered as broadly coeval with faulting along the CTZ  
162 (Figs. 2 and 3; Sibson et al., 1988; Bedeaux et al., 2017; Dubé, 2018), that is interpreted  
163 as a 1<sup>st</sup>-order structure to which 2<sup>nd</sup>- and 3<sup>rd</sup>-order structures are subordinate, the latter  
164 hosting most gold-bearing quartz-carbonate-tourmaline veins deposits of the Val-d'Or  
165 district (Robert, 1990; Neumayr et al., 1999). Hydrothermal alteration aureoles related to  
166 these shear zones and veins crosscut regional metamorphic isograds and destabilize the  
167 igneous and/or metamorphic minerals paragenesis of hosting rocks, attesting to a late- to  
168 post-metamorphic origin. The maximum age of the younger gold-rich hydrothermal event  
169 is constrained to <2680 Ma, based on U-Pb zircon ages from magmatic rocks hosting the  
170 mineralization at the Sigma-Lamaque deposit (see Neumayr et al., 1999). According to  
171 Robert et al. (2005), quartz-carbonate-tourmaline vein deposits postdated sedimentation  
172 of the Temiskaming Group and formed synchronously with regional metamorphism and  
173 late D<sub>2</sub> shortening at c. 2670-2660 Ma.

174

### 175 **3. Structural characteristics of the studied deposits**

176 For this study, we have mapped (or re-mapped) sections of the Lac-Herbin (Figs.  
177 4 and 5a), Beaufor and Beacon-2 mines (Figs. 5b and 5c). The Lac-Herbin and Beaufor  
178 mines (Lemarchand, 2012; Tessier, 1990; Tremblay, 2001) consist of 8 and 20  
179 underground levels, respectively, over a vertical distance of c. 400 and 650 metres,  
180 whereas the Beacon-2 deposit (Williamson, 2001) is a 2-level mine that is now used for  
181 educational underground mining and security purposes.

182 In each deposit (Figs. 4 and 5), moderately-to-steeply (40°–70°) south-dipping,  
183 East-West trending brittle-ductile reverse shear/fault zones filled with more-or-less  
184 continuous quartz-carbonate-tourmaline veins and associated subhorizontal  
185 extensional/sigmoidal flat veins host gold ore zones. All gold-hosting fractures were  
186 filled while the shear zones were still active and with the same veining material. Gold is  
187 associated with sulphides (mostly pyrite) and occurs within 1- to 2-metres-wide, sheared

188 and extensional quartz-tourmaline-sulphides-carbonate veins. Wallrocks are mylonitized  
189 granitic rocks hosting downdip stretching lineations and slickenside striae. The contact  
190 with the adjacent undeformed to slightly deformed plutonic rocks is marked by a gradual  
191 decrease in the intensity of mylonitization over a distance of 50 cm or less, and fault  
192 rocks vary accordingly from protomylonites to mylonites and ultramylonites from the  
193 margins toward the center of the shear zones. The rotation of the schistosity, and the  
194 presence of C-S fabrics, discontinuous shear bands, and folded extensional veins indicate  
195 a reverse sense of shearing. Mylonites and ultramylonites are fine grained, i.e., grains less  
196 than 0,1 mm in diameter. Feldspar porphyroclasts are present and occur within a matrix  
197 of ribboned chlorite-muscovite (sericite)-quartz-carbonate. Crystal-plastic textures in  
198 quartz grains and brittle fracturing of feldspars attest to brittle-ductile conditions of  
199 deformation at greenschist-grade conditions (350°–400°C; Passchier and Trouw, 1996).  
200 The mineralogy of the gold-bearing veins is typical of the greenschist facies ( $\leq 450^\circ\text{C}$ ).  
201 Beaudoin and Pitre (2005) proposed an average regional temperatures of 350°C during  
202 the formation of orogenic gold-veins in the Val d'Or mining district. This is in agreement  
203 with a minimum temperature estimate of 250-300°C for gold-bearing quartz veins at Lac-  
204 Herbin mine as suggested by Rezeau et al. (2017) who identified three unrelated fluid  
205 inclusion types, the oldest ones being related to the main filling stage of gold veins.  
206 These data are also consistent with temperature of 300-400 °C and 260-380°C reported  
207 by Robert and Kelly (1987) and Kerrich and King (1993), respectively, and with  
208 temperatures varying between 300°C and 450°C suggested for the Cadillac tectonic zone  
209 (Neumayr and Hagemann, 2002).

210 The structural analysis suggests that, at each mine site, the mineralized zones  
211 represent two or three gold-rich zones that were originally more or less continuous and  
212 dissected by a series of north-dipping, oblique-reverse dextral faults which lack evidence  
213 for pervasive hydrothermal alteration (Fig. 5; Tremblay, 2001; Lemarchand, 2012;  
214 Williamson, 2001). These barren, east-west-trending brittle faults which crosscut each  
215 deposit, are the Lac-Herbin-Sud fault at Lac-Herbin mine (Fig. 5a), the Perron and  
216 Beaufor faults at Beaufor mine (Fig. 5b), and the Beacon and New-Vein faults at Beacon-  
217 2 mine (Fig. 5c). Figures 5b and c shows that in the Beaufor and Beacon-2 mines, these

218 faults divide the deposits into a series of structural blocks between which it is difficult to  
219 correlate the auriferous zones. The width of the faults varies from 5 to 10 metres. They  
220 are marked by chlorite schist enclosing brecciated wall rock and barren quartz-chlorite  
221 veins. The chlorite schist is cut by discontinuous fractures filled by gouge material and/or  
222 cataclastic breccia. The large range of grain size in cataclasites, the limited  
223 recrystallization of quartz grains, and the predominance of intragranular fracturing and  
224 pressure solution attest to very low-grade conditions of deformation ( $\ll 300^\circ\text{C}$ ).

225

#### 226 **4. $^{40}\text{Ar}/^{39}\text{Ar}$ geochronology**

227 The establishment of unequivocal «absolute» ages for vein-type gold deposits is a  
228 subject of debate (e.g. Goldfarb et al., 2001; Robert et al., 2005). Among the isotopic  
229 dating methods (U-Pb, Sm-Nd,  $^{39}\text{Ar}$ - $^{40}\text{Ar}$ ) used to estimate the timing of orogenic gold in  
230 Archean terranes, a number of authors believe that the  $^{40}\text{Ar}/^{39}\text{Ar}$  method is less robust  
231 and yields ages that are often much younger than could seemingly be inferred by geologic  
232 facts. They consider such age results as minimum estimates (e.g. Kerrich and Cassidy,  
233 1994; Powell et al., 1995; Groves et al., 2000; Robert et al., 2005). We disagree with that  
234 statement and, in the following section, it will be argued that with the appropriate  
235 analytical approach and data representations, the  $^{40}\text{Ar}/^{39}\text{Ar}$  method yields age results that  
236 are consistent with a long-lasting incremental evolution of vein-type deposits. It is  
237 emphasized here, however, that a large number of  $^{40}\text{Ar}/^{39}\text{Ar}$  analyses is the best way to  
238 address the thermo-chronological evolution of complex natural systems such as vein-type  
239 orogenic deposits, which are characterized by a protracted and multistage structural and  
240 hydrothermal evolution during which the oldest radiogenic components are progressively  
241 obliterated by younger events, making their recognition difficult, sometimes impossible.

242 For this study, three types of rocks have been targeted for amphibole and mica  
243 single-grain  $^{40}\text{Ar}/^{39}\text{Ar}$  dating, (i) undeformed dioritic intrusions, (ii) mylonites derived  
244 from plutonic rocks hosting auriferous quartz-carbonate-tourmaline veins, and (iii)  
245 quartz-carbonate-tourmaline veins. 49 samples (55 analyses counting c. 1320 heating  
246 steps and c. 390 blanks for c. 700h of data acquisition) have been analyzed, most of them  
247 from the Lac-Herbin deposit (Lemarchand, 2012). To our knowledge, this is the most

248 extensive  $^{40}\text{Ar}/^{39}\text{Ar}$  geochronological study performed on a single orogenic gold deposit.  
249 Seven samples of amphibole come from the undeformed diorite at Lac-Herbin; 5 from  
250 underground workings and two from surface exposures (Fig. 6). Among the 42 samples  
251 of white mica, 26 are from the Lac-Herbin mine (Figs. 7 to 12), 7 from surface exposures  
252 of the Bourlamaque pluton in the vicinity of the Lac Herbin mine (Fig. 13), 6 from the  
253 Beaufor mine (Fig. 15) and 4 from the Beacon-2 mine (Fig.16). The overall distribution  
254 of white mica samples between quartz-carbonate-tourmaline veins and hosting shear  
255 zones is 60% and 40%, respectively. Whenever possible, the sampling of white mica  
256 pairs from quartz-carbonate-tourmaline veins and hosting mylonitic rocks has been  
257 favoured.

258

#### 259 *4.1 $^{40}\text{Ar}/^{39}\text{Ar}$ analytical method, data processing and presentation*

260 Samples were irradiated in two batches, IR14 and IR16, at McMaster Nuclear  
261 Reactor (Hamilton, Ontario, Canada) in its 5C high neutron flux facility. They  
262 respectively lasted 134.36h and 133.42 h with global efficiencies (J/h) of  $3.594 \times 10^{-4} \text{ h}^{-1}$   
263 and  $3.999 \times 10^{-4} \text{ h}^{-1}$ . Single grains of amphiboles and white micas (entire crystals or  
264 fragments) were analyzed by the  $^{40}\text{Ar}/^{39}\text{Ar}$  method in step-heating using a  $\text{CO}_2$  laser  
265 probe coupled with a MAP 215 mass spectrometer. The analytical procedure is described  
266 by Ruffet et al. (1991, 1995, 1997). The irradiation standard was amphibole Hb3gr  
267 (Turner et al. (1971); Roddick (1983); Jourdan et al. (2006) and Jourdan & Renne (2007)  
268 –  $1081.0 \pm 1.2 \text{ Ma}$  according to Renne et al. (2010) and Renne et al. (2011)). Blanks were  
269 performed routinely each first or third/fourth run, and subtracted from the subsequent  
270 sample gas fractions. Errors of apparent ages (ages of individual heating steps in age  
271 spectra which can be broken down into low, intermediate and high temperature apparent  
272 ages) are plotted at the  $1\sigma$  level and do not include the errors on the  $^{40}\text{Ar}^*/^{39}\text{Ar}_K$  ratio and  
273 age of the monitor and decay constant. Plateau ages were calculated if 70% or more of  
274 the  $^{39}\text{Ar}_K$  was released in at least three or more contiguous steps which define apparent  
275 ages agreeing, to within  $2\sigma$ , with the integrated age of the plateau segment. This 70%  
276 threshold, a requirement criterion that we use in all our geochronological studies, is much  
277 more restrictive than the 50% threshold set subjectively, in their own words, by Fleck et

278 al. (1977) and still adopted by most of the users of the  $^{40}\text{Ar}/^{39}\text{Ar}$  method. As the amount  
 279 of  $^{39}\text{Ar}_K$  released is not a disqualifying criterion, we have for a long time associated to  
 280 our restrictive age plateau concept used for "simple" mineral phases, the concept of  
 281 pseudo-plateau (Cheilletz et al., 1999), which meets the same statistical criteria except for  
 282 the cut-off threshold ( $<70\%$  of  $^{39}\text{Ar}_K$ ), and which is much more efficient for the analysis  
 283 of complex mineral phases. The errors on the  $^{40}\text{Ar}^*/^{39}\text{Ar}_K$  ratio and age of the monitor  
 284 and decay constant are included in the final calculation of the error margins on the  
 285 pseudo- and plateau ages.  $^{40}\text{Ar}/^{39}\text{Ar}$  ages are provided with  $1\sigma$  errors. Analytical data and  
 286 parameters used for calculations (e.g. isotopic ratios measured on pure K, Ca and Cl salts;  
 287 mass discrimination; atmospheric argon ratios; J parameter; decay constants) and  
 288 reference sources are available in the supplementary data repository.

289 Due to complexity of  $^{39}\text{Ar}$ - $^{40}\text{Ar}$  results of this study, especially for white micas,  
 290 their processing must go beyond the simple visual examination of age spectra. De Putter  
 291 et al. (2015) and De Putter and Ruffet (2020) presented and developed tools for the  
 292 visualization and processing of complex  $^{40}\text{Ar}/^{39}\text{Ar}$  systems governed by fluid inflows.  
 293 Three of these tools are classical: the plateau (Fleck et al., 1977) and pseudo-plateau age  
 294 (PPA) (Cheilletz *et al.*, 1999) concepts, and the probability density diagrams, which have  
 295 been first used for  $^{39}\text{Ar}$ - $^{40}\text{Ar}$  data by Deino & Potts (1992). Others tools are more  
 296 atypical; (i) the degassing and the weighted age spectra, which were designed to visualize  
 297 Ar degassing kinetics of  $^{40}\text{Ar}/^{39}\text{Ar}$  experiments, and (ii) the resizing of age spectra which  
 298 was developed to ensure their statistical representativeness. Because of their prominent  
 299 roles in this study, the two latter tools are described below.

300

301 *4.1.1 Degassing and weighted age spectra.* For  $^{40}\text{Ar}/^{39}\text{Ar}$  analyses of multi-component  
 302 systems, the kinetics of argon degassing can be visualized by means of a degassing  
 303 spectrum. The degassing spectrum reports for each step, vs.  $\%^{39}\text{Ar}_K$ , the amount of  $^A\text{Ar}$   
 304 (with mass number  $A=36$  to  $40$ ) weighted by the temperature difference with the previous  
 305 step ( $\Delta T^\circ$ ), this ratio being normalized between 0 and 1. It is expressed as  
 306  $(^A\text{Ar}/\Delta T^\circ)/(^A\text{Ar}/\Delta T^\circ)_{\text{Max}}$  versus  $\%^{39}\text{Ar}_K$  (with  $^A\text{Ar} = ^{40}\text{Ar}^*, ^{39}\text{Ar}_K, ^{37}\text{Ar}_{\text{Ca}}, ^{36}\text{Ar}_{\text{Atm}}$ ). A  
 307 degassing spectrum allows the visualization of variations in the degassing rate, thus

308 providing information on the isotopic/radiogenic components that may be present in the  
 309 analyzed material as well as on transitions between them during degassing. A  
 310 conventional age spectrum is a raw representation of the  $^{40}\text{Ar}/^{39}\text{Ar}$  experiment and does  
 311 not reflect variations in the degassing rate during the successive temperature increments.  
 312 Different steps corresponding to the same amount (Q) of  $^{39}\text{Ar}_K$  released will have the  
 313 same width on such spectra, regardless of the temperature increments ( $\Delta T^\circ$ ) that  
 314 produced them. The weighting of  $^{39}\text{Ar}_K$  degassing by temperature increments, expressed  
 315 by  $\%((^{39}\text{Ar}_K/\Delta T^\circ) / (^{39}\text{Ar}_K/\Delta T^\circ)_{\text{Max}})$ , yields a weighted age spectrum that integrates the  
 316 degassing rate and which is the result of the combination of the degassing spectrum and  
 317 the conventional age spectrum. On such spectra, the width of a step accounting for an  
 318 amount Q of argon released during a temperature increment  $\Delta T^\circ$  will be the same as that  
 319 of a step accounting for an amount x.Q of argon released during a temperature increment  
 320 x. $\Delta T^\circ$ . Hence, a weighted age spectrum allows depicting weakly expressed but clearly  
 321 identified radiogenic components (associated with degassing peaks) in proportion to their  
 322 degassing rates. Insofar as temperature ( $T^\circ$ ) measurement during  $\text{CO}_2$  laser probe analysis  
 323 is a major difficulty, the laser power control voltage ( $V_{T^\circ}$ ), a proxy indicator, is  
 324 substituted for it. Therefore, the degassing spectrum  $((^A\text{Ar}/\Delta V_{T^\circ})/(^A\text{Ar}/\Delta V_{T^\circ})_{\text{Max}}$  versus  
 325  $\%^{39}\text{Ar}_K$ ) and weighted age spectrum  $(\%((^{39}\text{Ar}_K/\Delta V_{T^\circ})/(^{39}\text{Ar}_K/\Delta V_{T^\circ})_{\text{Max}})$  would be used  
 326 only in order to identify radiogenic components in the analyzed materials and relate them  
 327 to the observed age spectra shapes, which implies that weighted age spectra should not be  
 328 directly used to calculate plateau or pseudo-plateau ages.

329

330 *4.1.2 The resizing of age spectra (Resized age spectra).* The use of probability density  
 331 diagrams involves ensuring that the age spectra that are compiled to construct them are  
 332 equally statistically representative. In such diagrams, all the heating steps contribute  
 333 almost equally since they are weighted by their respective errors but not by their  
 334 respective amount of degassed  $^{39}\text{Ar}_K$ .  $^{40}\text{Ar}/^{39}\text{Ar}$  experiments are never perfectly identical  
 335 (i.e. in terms of number of steps and % of  $^{39}\text{Ar}_K$  degassing per step) because the  
 336 degassing control is not perfect and analyzed samples are inevitably dissimilar. Resizing  
 337 the compiled age spectra is used to standardize their statistical representativeness in

338 probability density diagrams, thus ensuring that all age spectra have the same number of  
339 steps and that each step represents the same amount of  $^{39}\text{Ar}_K$  degassed. Such resizing of  
340 apparent ages obviously requires a reappraisal of their respective errors by respecting the  
341 principle of weighted averages.

342 Finally, it is important to prioritize the panel of tools presented above. Degassing  
343 spectra and weighted age spectra are basically a support to the interpretation of analyses,  
344 allowing data to be visualized in a different and more complete way. Conventional age  
345 spectra are at the heart of the validation process. They alone allow the statistical  
346 validation of significant ages through plateau and pseudo-plateau calculations which  
347 attest to the concordance of the apparent ages within a segment of the age spectrum and  
348 therefore to the isotopic coherence of the argon degassing for this domain, signaling the  
349 occurrence of a coherent radiogenic component. Probability density diagrams, either  
350 conventional or calculated after resizing the age spectra, are intrinsic validation tools  
351 since they represent the probability of occurrence of apparent ages for a given age range.  
352 They are also a synthetic representation of the validated ages.

353

#### 354 *4.2 Isotopic closures - from cooling to (neo/re)crystallization*

355 A radiochronological system is the combination of the crystal lattice of a mineral  
356 phase and an isotopic pair consisting of a radiogenic element and its radioactive  
357 precursor, e.g.  $^{40}\text{Ar}^*$  and  $^{40}\text{K}$ , the latter (K) being or not being a constituent of the lattice.  
358 The analysis of isotopic systems, particularly those involving noble gases, has long  
359 focused on the behaviour of the radiogenic element, in this case  $^{40}\text{Ar}^*$ , the host minerals  
360 being themselves considered inert and the fate of the isotopic system being exclusively  
361 governed by the diffusion of the gas under temperature control, as described by Fick's  
362 laws. This led to the notion of isotopic blocking temperature initially introduced by Jäger  
363 et al. (1967), formalized as the isotopic closure temperature ( $T_c$ ) by Dodson (1973) and  
364 then nuanced with the notion of isotopic closure window by Dunlap (1997). Therefore,  
365 during cooling and for a given isotopic system (mineral and isotopic pair), the isotopic  
366 chronometer initializes when diffusion becomes negligible because the temperature has  
367 dropped below its isotopic closure temperature.

368 Tc for amphibole is difficult to estimate. In addition to the effect of cooling rate  
369 and size of diffusion domains, amphibole diffusivity is also influenced by ionic porosity  
370 (Fortier and Giletti, 1989; Dahl, 1996). On the basis of natural hornblende compositions  
371 measured by various authors (i.e. Colville et al., 1966; Leake, 1978; Robinson et al.,  
372 1982), Dahl (1996) suggested a Tc range of 480-550°C, re-evaluated at 550-650°C by  
373 Villa (1998) using experiments of Kamber et al. (1995) suggesting that, depending on the  
374 crystal lattice characteristics, hornblende may form a closed system to Ar diffusion for  
375 temperatures as high as 580°C for cooling rates of 0.7°K/Ma (Villa et al., 1996).

376 Using experimental muscovite diffusion coefficients yielded by Harrison et al.  
377 (2009) and calculations performed by Pitra et al. (2010) with various effective diffusion  
378 radii (100 to 1000 µm) and cooling rates (1 to 1000°C/Ma), a 390-590°C temperature  
379 range could be estimated for white micas. White micas analyzed in this study are  
380 frequently sericite or poly-crystalline white mica (muscovite?) aggregates and it would be  
381 thus reasonable to consider lower isotopic closure temperatures, although it is difficult to  
382 quantify due to smaller effective diffusion radii than in well-crystallized muscovite  
383 crystals.

384 As shown by Cheilletz et al. (1999) and Alexandrov et al. (2002), in a context  
385 where deformation and/or fluid circulation are important parameters, the constituent  
386 mineral of the isotopic system is a weak link as it can evolve through partial or total static  
387 or dynamic recrystallization (*sensu lato*, i.e. in the broad sense of a process altering the  
388 crystal lattice) with a sequential reset of the  $^{40}\text{K}$ - $^{40}\text{Ar}$  couple at the scale of internal  
389 recrystallized zones. This process can lead to the coexistence of intra-crystalline domains  
390 with different chemical and isotopic compositions and thus distinct ages. Dunlap (1997)  
391 suggested that white micas from mylonites record neocrystallization related to ductile  
392 deformation at c. 350-250°C rather than cooling. The role played by hydrothermal fluids  
393 in the  $^{40}\text{K}$ - $^{40}\text{Ar}$  isotopic system is so significant that Villa (2010) stated, quote «*Mineral*  
394 *geochronometers should be viewed as «geohyrometers» that essentially date the fluid*  
395 *circulation episodes*». Tartese et al. (2011) exemplified this concept by evidencing  
396 sequential fluid-assisted resets of muscovite K-Ar isotopic chronometer during a time

397 span of 16 Ma after emplacement at shallow depth (3-6 km; Tartèse and Boulvais, 2010 )  
398 of a syn-kinematic leucogranite.

399 As amphiboles are part of the primary mineral paragenesis, they might potentially  
400 date emplacement/crystallization of the Boulamaque pluton, a small granitic body (23 x  
401 12 km), which foresees rapid cooling. Subsequent disturbing events, which may induce  
402 partial or total recrystallization of these primary amphiboles, arise after the pluton has  
403 cooled, below the amphibole isotopic closure temperature. White micas are part of a  
404 metamorphic minerals paragenesis and hydrothermal alteration which developed at  
405 greenschist facies conditions (see sections 2 and 3), below or at closing temperatures, and  
406 may record crystallization as old as the early stages of growth. Subsequent alteration(s) of  
407 the earliest white micas, detected by disturbed  $^{40}\text{Ar}/^{39}\text{Ar}$  age spectra with characteristic  
408 shapes (staircase, saddle; e.g. West and Lux, 1993; Dunlap, 1997; Cheilletz et al., 1999;  
409 Alexandrov et al., 2002; see section 5.2.1) would have occurred below isotopic closure  
410 temperature. The processing of these disturbed age spectra allows to estimate the age of  
411 partial/total recrystallization(s) which affected pre-existing minerals or to date the newly  
412 crystallized sub-grains (neocrystallization) aggregated with pre-existing ones.

413

## 414 5. RESULTS

### 415 5.1 Amphiboles

416 Typical  $^{40}\text{Ar}/^{39}\text{Ar}$  amphibole age spectra for undeformed diorite samples are  
417 shown in Figure 6. With the exception of sample TG-AMPH, all amphibole analyses  
418 were duplicated. JS-1 (a common diorite facies) and TG-AMPH (a differentiated diorite  
419 facies) were sampled at surface in the Lac-Herbin mine area, while the other five samples  
420 were taken at levels 15, 20, 25, 29 and 30 of the Lac-Herbin mine.

421 All amphibole age spectra from the surface down to level 20 are disturbed with  
422 either a staircase shape (e.g. J15-2 $\alpha$ ; Fig. 6e) or a saddle shape (e.g. JS-1 $\alpha$  and  $\beta$ ; Fig. 6c).  
423 These disturbances in age spectra generally correlate with a decrease of  $^{37}\text{Ar}_{\text{Ca}}/^{39}\text{Ar}_{\text{K}}$   
424 ratios ( $^{37}\text{Ar}_{\text{Ca}}/^{39}\text{Ar}_{\text{K}} = \text{CaO}/\text{K}_2\text{O} / 2.179$ ; Deckart et al., 1997) which reflect the chemical  
425 alteration of amphiboles, probably in relation to partial recrystallization. In spite of this,  
426 these amphiboles provide the oldest pseudo-plateau ages of this study, either in the high

427 temperature steps (e.g. J20-6 $\alpha$  and  $\beta$ ; Fig. 6f), or on sidewalls of saddles (e.g. JS-1 $\alpha$  and  
428  $\beta$ ; Fig. 6c). These  $^{40}\text{Ar}/^{39}\text{Ar}$  results allow the calculation of a mean age of  $2704.4 \pm 2.2$   
429 Ma (Figs. 6a and b), which is in good agreement with the zircon U-Pb age obtained by  
430 Wong et al. (1991) ( $2699.8 \pm 1.0$  Ma) for the Bourlamaque pluton. This coincidence of  
431 K-Ar and U-Pb ages as well as the above-mentioned isotopic closure temperatures of  
432 amphiboles suggest that the  $^{40}\text{Ar}/^{39}\text{Ar}$  age of c. 2700 Ma approximates the crystallization  
433 of amphiboles (Fig. 6b).

434 In contrast, amphiboles from the lowermost levels (25 to 30; Figs. 6g, h and i)  
435 yield less disturbed age spectra, which allow the calculation of plateau ages in the range  
436 2665-2668.5 Ma, with no evidence of the initial c. 2700 Ma crystallization stage. These  
437 amphiboles are characterized by  $^{37}\text{Ar}_{\text{Ca}}/^{39}\text{Ar}_{\text{K}}$  ratios in the order of 9.8-11.9, lower than  
438 those yielded by amphiboles of the uppermost levels (i.e. which yield  $^{37}\text{Ar}_{\text{Ca}}/^{39}\text{Ar}_{\text{K}}$  ratios  
439 of 13.7 to 17.1). These variations in ages and chemical composition (Ca/K ratios) as a  
440 function of depth (Fig. 6j), suggest that amphiboles from deeper domains were  
441 recrystallized during an event, labelled "event #1" on Figure 6b, which led to a total reset  
442 of their K-Ar isotopic system. This same event also explains partial recrystallizations  
443 expressed by staircase or saddle-shaped age spectra provided by some amphiboles  
444 collected at the surface (JS-1 $\alpha$  and TG-AMPH; Figs. 6c and d). A mean age of  $2666.9 \pm$   
445  $1.8$  Ma can be calculated for that event #1 (Figs. 6a and b). Most amphibole age spectra  
446 from levels 25 to 30 (Figs. 6g, h and i) also show a coherent disturbance in their low to  
447 intermediate temperature steps, at the expense of intermediate to high temperature ones  
448 which characterize event #1, with a corresponding pseudo-plateau ages bracket allowing  
449 the calculation of a mean age of  $2651.8 \pm 3.6$  Ma, labelled event #2 (Figs. 6a and b). This  
450 same perturbation could be also related to the saddle-shaped disturbance observed on  
451 amphibole age spectra of level 20 (Fig. 6f). Finally, saddle-shape spectra observed on two  
452 amphiboles from the surface (JS-1 $\beta$ ; Fig. 6c) and at level 25 (JSN25-4 $\alpha$ ; Fig. 6g) suggest  
453 the occurrence of a third, more discrete, disturbing event at  $2634.4 \pm 3.6$  Ma, labelled  
454 event #3 on Figure 6a.

455 Amphibole data are synthesized on Figure 6a and b, which emphasizes the timing  
456 of the three recrystallization events. Events #1 and #2 are primarily observed at the lower

457 levels of the Lac-Herbin mine. Recrystallizations deduced from the processing of  
458  $^{40}\text{Ar}/^{39}\text{Ar}$  analyses related to these events suggest that fluids, in disequilibrium with  
459 amphiboles, percolated at temperatures below their isotopic closure temperature. Our  
460 interpretation is that the crystallization of amphiboles occurred at ca. 2700 Ma, whereas  
461 the ca. 2666 Ma ages record a recrystallization event related to metamorphism. We admit,  
462 however, that events #1 and #2, at c. 2667 and c. 2652 Ma, possibly belong to a single  
463 geological event, which is regional metamorphism and syn- to late-orogenic plutonism  
464 related to the Preissac-Lacorne batholith. Event #3 can be related to the emplacement of  
465 the youngest phases of that same batholith, i.e. the ~2645 Ma Lamotte and Lacorne  
466 monzogranite plutons (Ducharme et al., 1997).

467

## 468 5.2 White micas

469 Scarce white micas found in sheared quartz veins are mostly sericite whereas  
470 those disseminated in the hosting shear zones are, with rare exceptions, poorly  
471 crystallized. Muscovite (*s.s.*) has only exceptionally been observed. Figures 7 to 14 show  
472 white mica age results obtained from the Lac-Herbin mine and surrounding surface area,  
473 whereas those for the Beaufor and Beacon-2 mines are shown in Figures 15 and 16,  
474 respectively.

475 The Lac-Herbin mine (Figs. 7 to 14) represents the vast majority of the white  
476 mica samples that were analyzed. It was sampled from levels 15 to 32 (150 to 370m  
477 depth), and seven surface samples were collected in the area surrounding the mine. The  
478  $^{40}\text{Ar}/^{39}\text{Ar}$  analyses were processed by grouping them by structures as follows, HW (Fig.  
479 7), S2 (Fig. 8), S1 (Fig. 9), S3 (Fig. 10), WE (Fig. 11), HW3 + Bonanza + Flat (Fig. 12).  
480 The analyses of the surface samples are shown in Figure 13 and all the results from the  
481 Lac Herbin area are synthetized in Figure 14. At the Beaufor mine (Fig. 15), samples  
482 were collected in zones C and F of level 1750 (533m depth) and in the vicinity of Dike 01  
483 fault zone (see Tremblay, 2001) whereas at the Beacon-2 mine (Fig. 16), the Canmet  
484 (Discovery) and New Vein structures were sampled on level 70 (70m depth). In the  
485 following, the names of samples taken at the Beaufor and the Beacon-2 mines begin with  
486 BF1750 and BC, respectively.

487           Among a total of forty-six  $^{40}\text{Ar}/^{39}\text{Ar}$  experiments carried out on white micas, only  
488 two (J15-2-WEa (Fig. 11) and BF1750-5a (Fig. 15)) allowed the calculation of plateau  
489 ages ( $\geq 70\%$  of  $^{39}\text{Ar}_K$  degassed). The remaining experiments produced multi-stepped age  
490 spectra with frequent staircase shape interspersed with one or more flat segments (e.g.  
491 J25-HW-QTZ-09; Fig. 7), more rarely, saddle shapes (e.g. J25-HW-MYL-09; Fig. 7), or  
492 a combination of both types of spectrum (e.g. BF 1750-7C; Fig. 15). As mentioned in  
493 section 4.1, the shape of age spectra expresses the partial re-crystallization of pre-existing  
494 grains or the aggregation of new (neo-formed) sub-grains that occurred after initial  
495 crystallization, below isotopic closure temperature, saddle shapes being associated with  
496 partial recrystallization whereas composite/aggregated mica grains usually produce  
497 stepped age spectra. The interpretation of these disturbed age spectra is intended to  
498 deconvolve the measured signal that expresses the coexistence and intermingling of  
499 multiple radiogenic components as illustrated hereafter through some characteristic  
500 examples. Six different radiogenic components, whose age decreases from c. 2650 Ma to  
501 c. 2450 Ma, have been identified and labelled as  $\alpha$ ,  $\beta$ ,  $\chi$ ,  $\delta$ ,  $\epsilon$  and  $\phi$ . They are illustrated  
502 hereafter through examples of characteristic age spectra found for white micas.

503

504 *5.2.1 Interpretative approach of  $^{40}\text{Ar}/^{39}\text{Ar}$  age spectra.* The following section aims at  
505 presenting the interpretative approach of disturbed age spectra yielded by most of our  
506 white micas  $^{40}\text{Ar}/^{39}\text{Ar}$  experiments through a few examples.

507           A saddle-shaped age spectrum obtained by  $^{40}\text{Ar}/^{39}\text{Ar}$  analysis of a single grain of  
508 white mica expresses the interaction between two radiogenic components whose  
509 coexistence results from partial recrystallization of a pre-existing material during a  
510 subsequent hydrothermal event (Cheilletz et al., 1999; Alexandrov et al., 2002;  
511 Castonguay et al., 2007; Tartèse et al., 2011; Tremblay et al., 2011). According to the  
512 interpretation proposed by Alexandrov et al. (2002), the apparent ages of the saddle edges  
513 in the low and high temperature steps provide a minimum estimate of the age of the pre-  
514 existing material whereas the apparent ages that define the base of the saddle provide a  
515 maximum estimate of the age of the event that induced partial recrystallization.  
516 Following this interpretative model, pre-existing radiogenic component of white mica

517 J25-HW-MYL-09 (Fig. 7), from a shear zone hosting the HW quartz vein at the Lac  
518 Herbin mine, would be as old as c. 2575 Ma. This "former" component will be referred to  
519 as  $\chi$ . Then, the mica grain has been partially recrystallized at the earliest around c. 2545  
520 Ma, which is also the age of a new radiogenic component, which will be referred to as  $\delta$ .

521 Most of our white mica analyses provided multi-stepped age spectra that express  
522 aggregations, via dissolution/recrystallization/neocrystallisation processes, of  
523 increasingly younger sub-grains as fluid inflows (hydrothermal pulses) occur.  $^{40}\text{Ar}/^{39}\text{Ar}$   
524 analyses of composite white micas thus produce complex degassing spectra with several  
525 degassing peaks (increased degassing rates), which may partially overlap, expressing  
526 more or less individualized and distinct radiogenic components. Furthermore, despite  
527 very detailed stepwise heating experiments, some sub-components of the analyzed grains  
528 are sometimes weakly expressed via classical representations (usual age spectrum)  
529 simply because they represent only a small proportion of the analyzed material. For these  
530 complex age spectra, the analysis of the argon degassing kinetics and the implementation  
531 of the weighting process (see section 4.1) allows to refine their interpretation. Hence,  
532 white mica J25-HW-QTZ-09 from a quartz vein hosted by the HW structure, yielded a  
533 typical multi-stepped age spectrum which shows two flat segments in the low and in the  
534 high temperature steps, but also a more discrete one in the intermediate temperature  
535 domain (Fig. 7). With the exception of the very low temperature steps (first 10% of  $^{39}\text{Ar}_K$   
536 released), the degassing spectrum shows three domains/peaks ( $\epsilon$ ,  $\delta$ ,  $\chi$ ), separated from  
537 each other by a drop in the degassing rate (Fig. 7), which characterize the degassing cycle  
538 of three distinctive sub-grains or isotopic components ( $\epsilon$ ,  $\delta$  and  $\chi$ ) within the composite  
539 mineral system represented by this sample. The degassing peaks/cycles  $\epsilon$  and  $\chi$  coincide  
540 perfectly with the two flat segments defined by the low and high temperature steps of the  
541 age spectrum. It is therefore reasonable to assign ages of  $2503.5 \pm 2.2$  Ma and  $2574.4 \pm$   
542  $3.7$  Ma, respectively, to these radiogenic components on the basis of pseudo-plateau ages  
543 that can be calculated from the corresponding flat segments of the age spectrum. The  
544 main degassing peak ( $\delta$ ) in the intermediate temperature domain is more complex.  
545 Apparent ages of the corresponding segment within the age spectrum increase steadily  
546 from c. 2505.5 Ma, matching perfectly the age of the low temperature component  $\epsilon$ , to a

547 flat segment for which a pseudo plateau age of  $2543.9 \pm 4.0$  Ma can be calculated (Fig.  
548 7). Assuming that this degassing peak is related to a component  $\delta$  with an age of c. 2544  
549 Ma, we may consider that it has been affected by partial recrystallization/dissolution  
550 during the growth of the younger  $\epsilon$  component. Nevertheless, it cannot be excluded that  
551 the onset of degassing peak  $\delta$  incorporates the tail of the low temperature degassing peak  
552  $\epsilon$  due to incomplete separation or partial overlapping between  $\epsilon$  and  $\delta$ . Under this  
553 assumption, the apparent age progression would simply reflect the transition from one  
554 component to the other ( $\epsilon \rightarrow \delta$ ).

555         Weighting the age spectrum of sample J25-HW-QTZ-09 (Fig. 7) by integrating  
556 the degassing rate doubles the width of the flat segment at c. 2544 related to component  
557  $\delta$ . The weighted age spectrum thus shows that, despite the moderate contribution to the  
558 overall  $^{39}\text{Ar}_K$  released, the signal produced by component  $\delta$  is of major importance in the  
559 shaping of the age spectrum. Similar mechanisms likely govern the transition between  
560 components  $\delta$  and  $\chi$  revealed by high-temperature steps, which is also associated with a  
561 small degassing peak (Fig. 7). The pseudo-plateau age calculated from the related flat  
562 segment of the spectrum suggests that component  $\chi$  could be as old as  $2574.4 \pm 3.7$  Ma.  
563 If, during transitions between components (e.g.  $\epsilon \rightarrow \delta$  or  $\delta \rightarrow \chi$ ), the above-mentioned  
564 partial recrystallizations/dissolutions remain limited, then the process of sub-grain  
565 aggregation (stepped age spectrum), allows a better preservation and identification of the  
566 oldest phases than after a pervasive partial recrystallization (saddle-shaped age  
567 spectrum), and the different radiogenic components are more easily separable during  
568 stepwise heating experiments.

569         Aggregations are sometimes less complex with coexistence of only two  
570 components as for white mica JSN17-4-HWb (Fig. 7). Its stepped age spectrum with flat  
571 segments in low to medium and in high temperature domains, associated with two  
572 distinct degassing peaks, results from the successive degassing of two radiogenic/mineral  
573 components. The weighting process highlights a first degassing sequence, related to a  
574 component labelled  $\chi$ , as old as  $2572.7 \pm 4.3$  Ma, because of its age concordance with the  
575 previously identified high temperature component of white mica J25-HW-QTZ-09. It is

576 followed by a second degassing sequence in high temperature domain which expresses  
577 the transition towards an older component, labelled  $\beta$ , as old as  $2602.5 \pm 7.8$  Ma.

578 A small proportion of the  $^{40}\text{Ar}/^{39}\text{Ar}$  age spectra combine stepped and saddle  
579 shapes. This is the case for our fourth example provided by white mica BF1750-7C (Fig.  
580 15) from a sheared quartz vein of zone C of the Beaufor mine. This analysis yielded an  
581 overall saddle shaped spectrum. However, in the low temperature steps ( $<10\%$  of  $^{39}\text{Ar}_K$   
582 released), it shows two small flat segments associated with degassing peaks attributed to  
583 sub-grains degassing. One of these peaks (labelled  $\beta$ ), between 5 and 10% of the  $^{39}\text{Ar}_K$   
584 released, is particularly well-expressed. The weighting process for this analysis amplifies  
585 that flat segment by a factor of 3, and a pseudo-plateau age at  $2600.8 \pm 6.8$  Ma can be  
586 calculated. The degassing of component  $\beta$  is preceded by that of component  $\chi$ , which is  
587 characterized by a small peak associated with a small flat segment in the age spectrum  
588 (between 2.5 and 5% of  $^{39}\text{Ar}_K$  released), allowing the calculation of a pseudo-plateau age  
589 at c. 2573 Ma (Fig. 15). This latter component  $\chi$  is substantial as it is also responsible for  
590 and constitutive of the saddle shape that characterizes most of the age spectrum. As  
591 previously explained, component  $\chi$  grows during hydrothermally-induced partial  
592 recrystallization of a pre-existing component, labelled  $\alpha$ , preserved in high temperature  
593 degassing domain of white mica BF1750-7C (Fig. 15) and at least as old as c. 2650 Ma.  
594 The latter component,  $\alpha$ , is also preserved in the high temperature steps of age spectrum  
595 yielded by white mica NW-DUM-5B (Fig. 13), which was collected from a surface shear  
596 vein in the vicinity of the Lac-Herbin mine. Sample NW-DUM-5B seems to be an  
597 aggregate/composite grain preserving, in addition to component  $\alpha$ , evidences for  
598 components  $\beta$  and  $\delta$  (Fig. 13), with component  $\beta$  partially recrystallized during an  
599 hydrothermal event that induced growth of younger component  $\delta$  (Fig. 13).

600 Both previous experiments show that younger components that grow at the  
601 expense of older ones during hydrothermally-induced partial recrystallizations ( $\chi$  at the  
602 expense of  $\alpha$  for BF1750-7C and  $\delta$  at the expense of  $\beta$  for NW-DUM-5B), form  
603 concomitantly as sub-grains aggregate with pre-existing ones. This suggests that partial  
604 recrystallization of pre-existing phases, growth of new components at the expense of pre-  
605 existing one and neocrystallization of new subgrains proceed concurrently through

606 dissolution-precipitation processes. Such an hypothesis explains why component  $\alpha$ ,  
607 which is the oldest that has been detected on white micas, is only exceptionally  
608 preserved, simply because the sequential and incremental hydrothermal evolution of the  
609 system gradually erases the oldest components, a process very similar to what has been  
610 described by De Putter and Ruffet (2020) for a  $^{40}\text{Ar}/^{39}\text{Ar}$  study of Mn oxides developing  
611 during the propagation of oxidation fronts in weathering profiles.

612

613 *5.2.2 Data synthesis.* All the identified components ( $\alpha$ ,  $\beta$ ,  $\chi$ ,  $\delta$ ,  $\epsilon$  and  $\phi$ ) were not  
614 simultaneously detected within a single white mica grain. Their presence in the analyzed  
615 white micas can be discontinuous, either because a given component is not detected or  
616 absent in a given experiment. However, three different components were frequently  
617 observed, exceptionally four. In fact, all experiments contain several radiogenic  
618 components, including the two analyses that allowed the calculation of plateau ages, both  
619 attributed to component  $\delta$ , i.e. white micas J15-2-WEa at  $2549.0 \pm 3.9$  Ma (a sheared  
620 wall rock of the WE zone of the Lac Herbin mine; Fig. 11) and BF1750-5a at  $2560.7 \pm$   
621  $3.3$  Ma (a quartz vein from zone E of the Beaufor mine; Fig. 15) which preserve former  
622 high temperature components  $\chi$  and  $\beta$ , respectively.

623 Among all these components,  $\alpha$  is the less well-preserved (see section 5.2.1). It  
624 has been, however, identified in two samples, NW-DUM-5B (Fig. 13) and BF1750-7C  
625 (Fig. 15), and could be as old as c. 2650 Ma.

626 Component  $\beta$  is well-represented among the analyses. It is the second oldest  
627 component with a mean age of c. 2597 Ma, and frequently appears as a high-temperature  
628 residual component in several age spectra. Component  $\beta$  is usually reworked by one or  
629 more younger age components, for instance;  $\chi$  in samples J15-2-S1a (S1 quartz vein; Fig.  
630 9) and JSN17-4-HWb (HW quartz vein; Fig. 7),  $\chi$  and  $\delta$  in samples JSN29-1-S2c (S2  
631 quartz vein; Fig. 8), JSN32-S1-QTZ-09 (S1 quartz vein; Fig. 9) and BC-CAN-09 (quartz  
632 vein in the Canmet (Discovery) Zone, Fig. 16),  $\chi$  and  $\epsilon$  in samples BC-NV-09 (New Vein  
633 Zone; Fig. 16) and MAP1-14 (surface shear zone; Fig. 13), or directly by component  $\delta$ ,  
634 without evidence for component  $\chi$ , as in samples J29-1/2-S2 (S2 quartz vein; Fig. 8),  
635 JR20-25-BZb (Bonanza quartz vein; Fig. 12) and BF1750-5A (Zone E quartz vein; Fig.

636 13).  $\beta$  is sometimes the principal component of the white mica which were analysed, as in  
637 samples JRPE-S2-QTZ-09 (S2 quartz vein; Fig. 8), BF1750-7A (Zone C shear zone; Fig.  
638 15), BC70-3 (New Vein Zone, Fig. 16) and NW-DUM-5B (Fig. 13).  $\beta$  is also present as a  
639 low-temperature component for sample BF1750-7C (Zone C quartz vein), in which it  
640 seems to be aggregated with component  $\alpha$ , both  $\beta$  and  $\alpha$  components being subsequently  
641 reworked by  $\chi$  (Fig. 15).

642 Component  $\chi$  is less well-expressed as compared to  $\beta$ , and yields ages clustering  
643 around 2575 Ma.  $\chi$  is detected as a high-temperature component of samples J25-HW-  
644 QTZ-09 (HW quartz vein; Fig. 7) and BC-CAN-09 (Fig. 16). It is also frequently  
645 observed in high-temperature steps and reworked by the  $\delta$ ,  $\varepsilon$  and sometimes  $\varphi$   
646 components in surface samples ADP-TOP-W, MAP5-35, MAP6-1 and SNBK-9B (Fig.  
647 13) and in J25-WE-QTZ-09 and J15-2-WEa white micas from a quartz vein and related  
648 shear zone of the WE structure (Fig. 11), in which it represents the oldest component.  $\chi$  is  
649 the main component in sample J25-HW-MYL-09 (Fig. 7), a shear zone hosting the HW  
650 quartz vein, or in samples J15-2-S1a and JSN32-S1-QTZ-09 (Fig. 9), JSN17-4-HWb  
651 (Fig. 7), JSN29-1-S2c (Fig. 8), MAP1-14 (Fig. 13), BC-NV-09 (Fig. 16), in which it is  
652 superimposed on component  $\beta$ . Finally,  $\chi$  is observed as a low temperature component, as  
653 well as associated with partial recrystallization of components  $\alpha$  and  $\beta$  within the white  
654 micas from quartz veins sample from Zone C at the Beaufor mine (BF1750-7C; Fig. 15)  
655 and from a S2 shear zone sample at Lac-Herbin (JRPE-S2-QTZ-09; Fig. 8).

656 Component  $\delta$  is undoubtedly of major importance among the white mica analyses  
657 performed during this study, suggesting that it could have had the strongest imprint.  $\delta$  has  
658 a mean age of c. 2551 Ma and is the only component that allowed the calculation of  
659 plateau ages, at  $2560.7 \pm 3.3$  Ma and  $2549.0 \pm 3.9$  Ma, from samples J15-2-WEa (Fig.  
660 11) and BF1750-5A (Fig. 15). Despite slight disturbances due to subsequent event  
661 associated with component  $\varepsilon$ ,  $\delta$  is also the main and oldest component identified in the  
662 age spectra of samples BF1750-5B (Zone E shear; Fig. 15) and BF1750-4 (Zone F quartz  
663 vein; Fig. 15). Component  $\delta$  is detected in high-temperature steps for a very large number  
664 of analyses, and is affected to varying degrees by younger components  $\varepsilon$  and  $\varphi$ . This is  
665 particularly well shown by mica samples of a S1 quartz vein (J15-2-S1b) and related

666 shear zone (JSN32-S1-MYL-09 and J25-8-S1) (Fig. 9). The same is true for all quartz  
667 vein samples of zones S3 (J29-1-S3, JSN25-4-S3b and J29-2-S2/S3; Fig. 10) and WE  
668 (J15-2-WEb and J25-WE-QTZ-09; Fig. 11). For S3 shear zone and quartz veins, it is the  
669 oldest component detected in their respective age spectra. Similar results are also found  
670 in quartz vein samples from surface exposure (SG-3; Fig. 13), and from the Beacon-2 and  
671 Beaufor mines (BC70-1A and BF1750-1D, respectively; Fig. 15 and 16).  $\delta$  is only rarely  
672 observed in low temperature heating steps of age spectra, although it is clearly detected  
673 as such in sample JSN29-1-S2c (a S2 quartz vein; Fig. 8) and in two surface samples  
674 (quartz vein NW-DUM-5B and shear MAP1-14; Fig. 13).

675         Components  $\epsilon$  and  $\phi$  are mostly observed in low and intermediate temperature  
676 steps of age spectra. These are the two youngest components detected during this study,  
677 with mean ages of c. 2500 Ma for  $\epsilon$  and c. 2452 Ma for  $\phi$ . There are only two age spectra  
678 characterized by component  $\epsilon$  in high-temperature steps, J30-S3 and J25-4-HW3 from  
679 shears S3 (Fig. 10) and HW3 (Fig. 12), respectively, which show no evidence for older  
680 components. The imprint of component  $\epsilon$  is particularly well-detected in the intermediate  
681 temperature domain, and is a much stronger signal as compared to component  $\phi$ .

682         When a large set of data is available, the use of probability density diagrams  
683 (frequency diagrams) is appropriate. As mentioned in section 4.1, frequency diagrams are  
684 used to determine the probability of occurrence of a given apparent age for each age  
685 sampled (at a 1 Ma frequency interval in our study), and provide a synthetic view of the  
686 distribution of apparent ages. Plateau and pseudo-plateau ages were compiled for the  
687 three studied mines and compared with the probability density diagrams of apparent ages  
688 (Figs. 14, 15 and 16). Hence, for the Lac-Herbin (Fig.14) and Beacon-2 mines, the  
689 probability density diagrams show a perfect age concordance for 5 of the 6 components  
690 mentioned above. With the exception of component  $\phi$ , the age of components identified  
691 in these two mines is in agreement with frequency peaks of apparent ages as defined by  
692 their respective frequency diagrams (Figs. 14 and 15). The adequacy between validated  
693 ages and frequency peaks of apparent ages is less clear for the Beaufor mine, which can  
694 be due to a limited representativeness of the small number of samples from this mine.

695 While adequacy between the frequency peaks and the statistically validated ages  
696 (plateau and pseudo-plateau ages) is a factor of internal consistency and validation, the  
697 reverse is not a disqualifying factor. Biases can be induced by transition domain, within  
698 age spectra, between significant segments which will characterize distinct radiogenic  
699 components. This could be the case at the Lac Herbin mine for the two youngest  
700 components ( $\varphi$  and  $\varepsilon$ ). Moreover, as the origin (partial recrystallization vs. aggregation)  
701 of the multiple radiogenic components present within a white mica grain governs the  
702 relations between them and thus the shape of the age spectra they generate (saddle or  
703 stepped shapes), it also controls the shape of the resulting frequency histograms. The high  
704 prevalence of partial recrystallization within the white mica from the Beaufor mine could  
705 explain the discrepancy between the estimated ages of components  $\varepsilon$ ,  $\delta$ ,  $\chi$  and  $\beta$  and the  
706 frequency peaks of apparent ages. This emphasizes the fact that a frequency histogram is  
707 not always a panacea, and that it must be handled with discernment and that data  
708 processing requires a careful degassing analysis and statistical validation by calculating  
709 plateau and pseudo-plateau ages.

710 Nevertheless, the age of the six components that were identified among the white  
711 mica spectrum are clearly distinct, with no overlaps (Fig. 17). They cover a time period  
712 of approximately 200 m.y., starting around c. 2651 Ma (component  $\alpha$ ), followed by 3  
713 successive phases (components  $\beta$ ,  $\chi$  and  $\delta$ ) that peak with a period of c. 20-25 Ma at c.  
714 2597 Ma (component  $\beta$ ), 2575 Ma (component  $\chi$ ) and 2551 Ma (component  $\delta$ ), these  
715 three phases probably representing the paroxysm of hydrothermal activity since they left  
716 the strongest imprints in the study area. This is followed by two younger phases,  
717 associated with component  $\varepsilon$  ca. 50 m.y. later (at c. 2500 Ma) and component  $\varphi$ , another  
718 ca. 50 m.y. later (at c. 2452 Ma).

719 The errors attributed to the mean ages of the various components (Figs. 14, 15, 16  
720 and 17) have no other meaning than standard deviations, because the age distributions  
721 observed for each component may be the expression of "analytical" dispersions as well as  
722 the duration of events.

723

## 724 6. DISCUSSION

725 *6.1 Validation of  $^{40}\text{Ar}/^{39}\text{Ar}$  ages*

726 As most  $^{40}\text{Ar}/^{39}\text{Ar}$  experiments, at least for white micas, suggest a mixing between  
727 different radiogenic components, one may question if the deconvolution of results is  
728 adequate. A systematic consistency between the ages of the distinct radiogenic  
729 components identified in amphibole and/or white mica grains suggests that it has been the  
730 case and this is the reason why some of them have been similarly labelled for different  
731 analyses. We think that this indicates that the  $^{39}\text{Ar}$ – $^{40}\text{Ar}$  age results have a regional  
732 geochronological and geological significance. Besides, the estimated age of component  $\alpha$   
733 (c. 2650 Ma) identified in white micas is consistent with the age of event #2 recorded by  
734 amphiboles (see Fig. 17), suggesting that the crystallization of this first generation of  
735 white micas in shear-related veins has been synchronous with the partial  
736 reset/recrystallization of amphiboles in the hosting rocks of the Bourlamaque pluton. The  
737 subsequent disturbing events preserved in white micas (i.e. components  $\beta$  to  $\varphi$ , from c.  
738 2600 Ma down to c. 2450 Ma) are not recorded by amphiboles. On the other hand, the  
739 absence of components older than  $\alpha$  in white micas, whether due to a complete  
740 obliteration or the non-existence of earlier components, precludes the establishment of  
741 genetic links between white micas and amphiboles prior to c. 2650 Ma, i.e. especially  
742 with respect to disturbance event #1 (c. 2667 Ma) recorded by amphiboles.

743  $^{40}\text{Ar}/^{39}\text{Ar}$  ages measured during this study cannot be attributed to the passive  
744 erosional exhumation of the AGB, in which case any given mineral species shall yield,  
745 within errors, the same range of ages, which is obviously not the case. Amphibole ages  
746 that cluster at ca. 2704 Ma overlap, within errors, with the U-Pb zircon age of the  
747 Bourlamaque pluton and are interpreted as magmatic cooling ages, close to crystallization  
748 (Figs. 6 and 17). Amphibole ages at c. 2667 Ma yielded by some plateau spectra and  
749 saddle-shaped perturbations can be attributed to regional peak metamorphism and/or syn-  
750 orogenic magmatism (Fig. 18), more likely coeval with the emplacement of the  
751 monzodioritic suite (2690–2670 Ma; e.g. Daigneault et al., 2002) of the Preissac-Lacorne  
752 batholith (Fig. 2). The partial or complete rejuvenation of  $^{40}\text{Ar}/^{39}\text{Ar}$  amphibole ages with  
753 depth (over a vertical distance of approximately 300 metres) at Lac-Herbin (Fig. 6) is  
754 worthy of discussion. Obviously, these rejuvenating events, clustering at ca. 2665, 2650

755 and perhaps 2635 Ma (Fig. 6a), cannot be attributed to deformation since these  
756 amphibole samples were taken away from mineralized shear zones. We think that there  
757 are three possible explanations. (1) Age variations are due to progressive exhumation by  
758 erosion, and surface samples therefore crossed the  $T_c$  for amphibole earlier than those at  
759 depth. As argued above, this is unlikely since similar age-depth relations are not shown by  
760 white mica samples. (2) There is an intrusive body at depth that is the cause of local  
761 thermal perturbations of the  $^{40}\text{Ar}/^{39}\text{Ar}$  amphibole system; there is no geophysical and/or  
762 lithological evidence for shallow intrusions in either of the gold deposits hosted by the  
763 Bourlamaque pluton, and we thus consider that hypothesis as unlikely. (3) Amphibole  
764 spectrum perturbations are due to mineral recrystallization related to pervasive fluid  
765 impregnation, which would have been coeval with regional metamorphism and/or  
766 emplacement of monzodioritic (c. 2690-2670 Ma) and granitic (c. 2660-2642 Ma) suites  
767 of the Preissac-Lacorne batholith, or both, an hypothesis that we prefer and which is more  
768 consistent with white mica results.

769 The  $^{40}\text{Ar}/^{39}\text{Ar}$  analyses of white micas identified 5 radiogenic/mineral components  
770 whose mean ages decrease from c. 2600 Ma down to c. 2450 Ma. (Fig. 17). We believe  
771 that these ages are geologically significant because (1) white mica  $^{40}\text{Ar}/^{39}\text{Ar}$  plateau and  
772 pseudo-plateau ages are consistent at the scale of the Bourlamaque pluton, i.e. similar  
773 plateau and pseudo-plateau ages were obtained in different deposits, (2) pairs of vein- and  
774 mylonite-hosted micas yielded overlapping plateau and pseudo-plateau ages, which is, for  
775 instance, consistent with the Sibson's et al. (1988) fault-valve model of coeval  
776 deformation and fluid circulation, and (3) there is very good consistency between the  
777 apparent age frequency peaks and the plateau and pseudo-plateau ages provided by  
778 samples from the Lac Herbin and Beacon-2 mines, but less so at the Beaufor mine for  
779 reasons mentioned above. The 5 identified components record sequential  
780 dissolution/recrystallization /neocrystallization/aggregation processes that affected white  
781 micas during at least 150 m.y., and that testify to dynamic recrystallization processes  
782 during peak periods of more-or-less intense fluid circulation and deformational events  
783 (Fig. 17). However, as discussed in the following section, the question remains regarding

784 the fertility of these hydrothermal events in terms of gold entrapment in associated  
785 structures.

786

### 787 *6.2 Age and duration of gold-vein formation in the Val d'Or mining district*

788 The oldest evidence for fluid circulation in the Bourlamaque pluton is recorded by  
789 amphiboles with ages within the age bracket inferred for the peak of regional  
790 metamorphism and emplacement of the Preissac-Lacorne batholite, whereas the youngest  
791 evidence is yielded by  $^{40}\text{Ar}/^{39}\text{Ar}$  muscovite ages around 2450 Ma from quartz-veins  
792 and/or hosting mylonites (Fig. 18). There is no magmatic muscovite in the Bourlamaque  
793 pluton, and all muscovite/sericite minerals and/or aggregates analysed during this study  
794 are related to fluid circulation/alteration driven by incremental shearing deformation.  
795 Obviously, the development of quartz-carbonate-tourmaline vein systems hosted by the  
796 Bourlamaque pluton has been also incremental. We cannot be sure that hydrothermal  
797 fluids circulation generated during regional metamorphism (ca. 2670-2660 Ma) and/or  
798 emplacement of the old (2690-2670 Ma) and young (2660-2642 Ma) plutonic suites of  
799 the Preissac-Lacorne batholith, if any, has been coeval with the formation of auriferous  
800 quartz veins. However, the identification of a radiogenic/mineral component of white  
801 mica as old as c. 2650 Ma (Fig. 18) favors the onset of gold entrapment in the  
802 Bourlamaque pluton (and the Val d'Or mining district *in extenso*) coeval, at the earliest,  
803 with a corresponding hydrothermal stage referred to as  $\alpha$  on Figure 18. Although the  
804 progressive deformation and dynamic recrystallization induced by multiple hydrothermal  
805 pulses precluded the preservation of most of the white mica that may have initially  
806 crystallized concomitantly with the initiation of gold vein, say in the 2670-2660 Ma  
807 range, we argue that gold vein formation occurred no earlier than c. 2650 Ma. In the Lac-  
808 Herbin deposit, this component  $\alpha$  would correspond to type 1 gold-bearing, aqueous-  
809 carbonic fluid inclusions identified by Rezeau et al. (2017) which were generated,  
810 according to them, during regional metamorphism.

811 Following the early stage  $\alpha$ ,  $^{40}\text{Ar}/^{39}\text{Ar}$  muscovite ages define 4 other well-  
812 expressed frequency peaks covering a time period of approximately 100 m.y. (Fig. 18), at  
813 c. 2597 Ma (stage  $\beta$ ), c. 2575 Ma (stage  $\chi$ ), c. 2551 Ma (stage  $\delta$ ), c. 2500 Ma (stage  $\epsilon$ ),

814 and a more discrete one at c. 2452 Ma (stage  $\phi$ ). The spreading of  $^{40}\text{Ar}/^{39}\text{Ar}$  ages from c.  
815 2650 Ma down to c. 2500 Ma (Fig. 18) suggests that localized shear deformation and  
816 related gold mineralization and/or remobilization in the Val d'Or mining district may  
817 have lasted for more than 150 m.y., which is significantly longer than suggested in  
818 current literature. At the Lac-Herbin deposit, Rezeau et al. (2017) identified three  
819 unrelated fluid inclusion types in the main vein filling ore stage, (1) aqueous-carbonic  
820 inclusions interpreted to have formed during regional metamorphism (corresponding to  
821 our component  $\alpha$ ) and to represent gold-bearing fluids, (2) barren high-temperature,  
822 aqueous, moderately saline inclusions postdating type 1 inclusions, and considered as a  
823 remobilizing agent of earlier precipitated gold, and (3) barren low-temperature, aqueous,  
824 high saline inclusions similar to crustal brines reported throughout the Canadian Shield  
825 and considered to be unrelated to orogenic gold mineralization (e.g. Boullier et al., 1998).  
826 The age of fluid inclusions studied by Rezeau et al. (2017) is unknown and, since the  
827 sampled structures are not identified in their study, it is impossible to make any  
828 connection with  $^{40}\text{Ar}/^{39}\text{Ar}$  data from the Lac-Herbin deposit. Interestingly, Rezeau et al.  
829 (2017) argued that type 2 fluid inclusions represent a different hydrothermal fluid  
830 emplaced after and at higher temperature (as compared to type 1), that acted as a  
831 remobilizing agent for previously precipitated gold. They suggested that these fluids were  
832 generated during and/or following the emplacement of S-type granitic intrusions of the  
833 Preissac-Lacorne batholith at ca. 2645-2611 Ma. This is basically consistent with our  
834 genetic model of multistage tectonothermal events, and we suggest that gold  
835 introduction/remobilization continued for a long time period after the final stages of post-  
836 orogenic magmatism, most probably due to a slow cooling rate of the Archean  
837 lithosphere (e.g. Willigers et al., 2002; and references below).

838 Our  $^{40}\text{Ar}/^{39}\text{Ar}$  results are consistent with other geochronological evidence for  
839 «young» Au-rich hydrothermal fluid circulation that have been obtained with different  
840 isotopic tools in the Val d'Or mining district and adjacent areas of the southern Abitibi  
841 Belt (Fig. 18). Gold mineralization ages of  $2633 \pm 3$  Ma,  $2627 \pm 2$  Ma and  $2600 \pm 3$  Ma  
842 have been obtained by U-Pb dating of hydrothermal rutile, sphene and titanite,  
843 respectively, at the Camflo mine (Jemielita et al., 1990; Zweng et al., 1993). In the Sigma

844 mine, Wong et al. (1991) measured a U-Pb age of  $2599 \pm 9$  Ma on a hydrothermal rutile.  
845 Sm-Nd analyses of scheelite and tourmaline from Sigma, Perron and Sisco deposits  
846 yielded isochron ages of  $2596 \pm 33$  Ma and  $2593 \pm 18$  Ma (Anglin et al., 1996), whereas  
847 Olivo et al. (2007) measured a Pb-Pb age of  $2566 \pm 71$  Ma from hydrothermal pyrites in  
848 the Sisco deposit. Hanes et al. (1992) reported a  $^{40}\text{Ar}/^{39}\text{Ar}$  muscovite age of  $2579 \pm 9$  Ma  
849 from a quartz-tourmaline vein at the Sigma mine, arguing that this was a minimal age for  
850 mineralization. Zweng et al. (1993) argued that these  $^{40}\text{Ar}/^{39}\text{Ar}$  ages record closure during  
851 post-2640 Ma cooling but, according to Corfu (1993), it is also possible that some of the  
852 observed age variations record late and localized pulses of hydrothermal activity.  
853 Moreover, Sasseville and Jebrak (2017) recently measured  $^{187}\text{Re}/^{187}\text{Os}$  isochrons  
854 clustering at c. 2575, c. 2505, c. 2398 and c. 2267 Ma from various gold deposits of the  
855 Val d'Or area, the latter two age clusters being tentatively attributed to thermal pulses  
856 and gold remobilization related to the Matachewan Igneous Province.

857 At the scale of the Superior Province, there is accumulating geochronological  
858 evidence for major crustal deformation event(s) and related metamorphism spreading  
859 over a timeframe much larger than suggested in literature (e.g. Percival (2007), for  
860 instance), that described the Superior Province as a succession of five orogenic events  
861 which propagated southward from 2.72 to 2.68 Ga. In Ontario, Easton (2000) argued that  
862 the distribution of metamorphic grade and age of metamorphism reflects a series of  
863 tectonic events between 2710 and 2640 Ma, which followed the early accretion (between  
864 2720 and 2690 Ma) of different oceanic terranes (arcs, back-arcs) and microcontinents.  
865 Such a time interval (2710-2640 Ma) is in agreement with U-Pb zircon age constraints for  
866 metamorphism, syn-orogenic magmatism and deformation in the Val d'Or mining district  
867 (Fig. 18). It is also consistent with  $^{40}\text{Ar}/^{39}\text{Ar}$  age data from the northern Abitibi Belt and  
868 the adjacent Opatoca Plutonic Belt (OPB) where amphibole and micas ages record a  
869 metamorphic history starting at c. 2685 Ma and vanishing around 2630 Ma (Daoudene et  
870 al., 2014; 2016). To the north of the OPB, in the Opinaca subprovince, granulite-facies  
871 regional metamorphism spreads over ages varying from c. 2666 Ma to 2636 Ma (Morfin  
872 et al., 2013). Metamorphism even lasted down to ca. 2620-2600 Ma in supracrustal rocks  
873 of the La Grande subprovince (Fontaine et al., 2017; 2018). Combined with

874 geochronological data from the southern Abitibi belt, this is a strong indication that peak  
875 and duration of regional metamorphism have been more-or-less coeval over a large  
876 region, if not all over the Pontiac, Abitibi and Opatoca subprovinces and beyond.

877

### 878 *6.3 Tectonic implications for Archean orogenic gold deposits.*

879 In the Superior Province of Ontario, Easton (2000) suggested that relationships  
880 between subprovince type, metamorphic grade and geochronological ages show that  
881 granite-greenstone domains (such as the AGB) preserves old greenschist- to lower-  
882 amphibolite-facies metamorphic event(s) whereas high-grade gneiss domains (such as the  
883 OPB) preserves the youngest metamorphic events. This was interpreted to be consistent  
884 with a «deep-later» model of gold mineralization (e.g. Stüwe, 1998), in which gold-  
885 bearing fluids and pegmatite-forming melts develop, at least in part, during prograde  
886 granulite-facies metamorphism/magmatism (and devolatilization) in the lower crust and  
887 are structurally-trapped (as «post-metamorphic» quartz veins and dikes) during ascension  
888 to shallow crustal levels (see also Krogh, 1993). Presently, there are not sufficiently  
889 abundant and largely distributed metamorphic age data in the Quebec Superior Province  
890 to support Easton's (2000) proposition. Metamorphic grade variations in the AGB (Faure,  
891 2015) indicates, however, that metamorphic isograds increase progressively from the  
892 uppermost towards the lowermost crustal sequences of both the Abitibi and Opatoca belts;  
893 orthogneisses of the Opatoca Plutonic Belt (OPB) are at amphibolite- to granulite-facies  
894 (Sawyer and Benn, 1993; Daoudene et al., 2016) whereas the lower part of the AGB is at  
895 amphibolite facies and its uppermost sequences at greenschist- and lower grade,  
896 indicating that metamorphism increases with crustal depth (Daoudene et al., 2016;  
897 Tremblay et al., 2019). Faure's (2015) metamorphic compilation also indicates that  
898 metamorphic isograds are essentially subhorizontal in the AGB, in which higher-grade  
899 metamorphic rocks occur within and around TTG complexes that essentially represent  
900 structural windows exposing OPB-like lower crust orthogneisses.

901 An increasing volume of continental crust and crustal fluid production towards the  
902 end of the Archean (e.g. Condie et Benn, 2006; Sizova et al., 2010) and a higher  
903 geothermal gradient and fluid convection efficiency can have accounted for multiple, ~10

904 m.y.-long peaks of hydrothermal activity in the Val d'Or mining district (Fig. 18).  
905 Connolly (2010), for instance, argued that metamorphic fluids in the crust are expelled by  
906 hydrothermal pulses/batches along fracture/fault zones, which is conceptually consistent  
907 with the sequence of frequency peaks of  $^{40}\text{Ar}/^{39}\text{Ar}$  ages highlighted for the Bourlamaque  
908 pluton. It is therefore reasonable to propose that the time periodicity of hydrothermal  
909 pulses recorded by our  $^{40}\text{Ar}/^{39}\text{Ar}$  data is a direct consequence of physical processes  
910 responsible for the formation of these vein systems, although we cannot be sure that  
911 every hydrothermal pulse has been recorded. A succession of tens to thousands of  
912 hydrothermal pulses over a period of 100 m.y., or more, implies the incremental and  
913 repetitive precipitation and/or remobilization of auriferous sulphides and native gold.  
914 Incidentally, several gold occurrences of the Val d'Or district preserve evidence for  
915 multiple generations of gold influx within a single deposit (Robert and Brown, 1986;  
916 Robert and Kelly, 1987; Roussy, 2003; Olivo et al., 2006; Rezeau et al., 2017).

917 As mentioned above, in the Val d'Or mining camp, the Cadillac tectonic zone  
918 (CTZ) is currently considered as a 1<sup>st</sup>-order structure that drained hydrothermal fluids  
919 towards 2<sup>nd</sup>- and 3<sup>rd</sup>-order shears (e.g. Neumayr et al., 1999) such as the ones hosting  
920 gold mineralization in the Bourlamaque pluton. Do our  $^{40}\text{Ar}/^{39}\text{Ar}$  data mean that faulting  
921 increments along the CTZ continued to be active long after the end of regional  
922 metamorphism (i.e. post-ca. 2630 Ma)? Is it reasonable to infer more-or-less localized  
923 hydrothermal and faulting activity along the CTZ during 150 m.y., if not more? The CTZ  
924 is a 250 km-long high-strain zone (Fig. 2) that had a complex structural evolution with  
925 successive shortening, extensional and late strike-slip faulting events (e.g. Daigneault et  
926 al., 2002). Bedeaux et al. (2017) published a very detailed structural analysis of the  
927 Rouyn-Val d'Or segment of the CTZ, arguing that the latest dextral strike-slip fault  
928 increments occurred at c. 2665 Ma and were coeval with the emplacement of major  
929 orogenic gold deposits, such as those of the Val d'Or district. Their timing hypothesis is,  
930 however, poorly constrained as it basically relies on selected isotopic ages from the Val  
931 d'Or area (as compiled by Robert et al., 2005) and on U-Pb dating of the syn-kinematic  
932 Murdock Creek and Lebel stocks in the Kirkland Lake area, Ontario (Wilkinson et al.,  
933 1999), 200 km west of the Val d'Or district. Long-lasting faulting and variations of the

934 kinematic frame of a single crustal-scale structure are common; for instance, the Alpine,  
935 San Andreas and North Anatolian faults, which are often used as modern equivalents to  
936 the CTZ, have been active since c. 25, 30 and 43 m.y., respectively (Lamb, 2011; Popov  
937 et al., 2012; Nuriel et al., 2019). These are minimal values for the duration of deformation  
938 along these crustal faults. The North Anatolian fault, for instance, is a long-lived fault  
939 system that formed during multiple events and by reactivation of pre-existing fault  
940 systems, the present dextral style of deformation being active since at least 11 m.y.  
941 (Nuriel et al., 2017).

942 Finally, it is worth discussing the implications of the  $^{40}\text{Ar}/^{39}\text{Ar}$  dating of  
943 auriferous structures of the Bourlamaque pluton for the relative timing of barren veins  
944 and east-west trending brittle faults that cut across gold mineralization at each of the  
945 studied deposits, i.e. the Perron, Beaufor, New Vein, Beacon and Lac Herbin-Sud faults  
946 (see Fig. 5). We emphasize here that these faults expose fabrics that contrast sharply with  
947 gold-related structures, as they are essentially characterized by brittle to brittle-ductile  
948 deformation features, sub-horizontal lineations, and bear no evidence for intense  
949 hydrothermal activity during faulting. Such structures also exist elsewhere in the Val  
950 d'Or mining district as, for instance, the K-Zone at the Siscoe deposit (Sauvé et al., 1993)  
951 and the Dunraine shear (Daigneault, 1996; Moorehead et al., 1998) which fringes the  
952 Louvicourt massive sulfide deposit. The orientation and structural characteristics of shear  
953 zones and late brittle faults preserved in the Bourlamaque pluton are reminiscent of  
954 regional tectonics in the Val-d'Or mining district where the CTZ show evidence for both  
955 reverse and dextral strike-slip movement, attributed to different increments of faulting  
956 (Bedeaux et al., 2017) or dextral transpression during progressive deformation (Robert,  
957 1989). Fault structures within the studied gold deposits suggest, however, that reverse  
958 and dextral transcurrent faulting are genetically unrelated and probably resulted from  
959 sequential faulting. After an undetermined period of time following gold mineralization,  
960 long enough to annihilate significant fluid circulation and allow the transition to brittle  
961 conditions of deformation, strike-slip faulting was initiated in the Val d'Or mining  
962 district and various sets of faults, crosscutting the pre-existing shears and veins, were  
963 formed. If correct, this means that strike-slip fault formation and/or reactivation has been

964 coeval with or younger than ca. 2500-2450 Ma (latest Archean) hydrothermal events.  
965 Interestingly, Kaminemi et al. (1990) described similar brittle structures and cataclastic  
966 faults with Rb/Sr ages of 2300 Ma (Early Proterozoic) cutting Late Archean granitic  
967 plutons in the western Superior Province; they argued that this is evidence that structural  
968 disturbance of the internal Superior craton did not terminate with plutonism at the end of  
969 the Kenoran orogeny but continued intermittently for at least several hundred millions  
970 years, possibly in response to events taking place beyond margins of that craton.

971

## 972 7. CONCLUSION

973 The large amount of  $^{40}\text{Ar}/^{39}\text{Ar}$  analyses produced during this study has raised  
974 important implications to be made on the different veins and shear structures that were  
975 sampled. The whole geochronological dataset obviously reflects the final state of the  
976 different auriferous shear zones systems. Hydrothermal components expressing previous  
977 states potentially existed before being obliterated, as it is the case for component  $\alpha$  (c.  
978 2650 Ma) which has been only locally detected and almost totally erased by intense  
979 hydrothermal/tectonic activity at c. 2600-2550 Ma (Fig. 18). In the Lac-Herbin deposit,  
980 the preserved hydrothermal history started around c. 2600 Ma with the crystallization of  
981 component  $\beta$  along most structures, at the exception of WE and HW3 which may have  
982 been initiated later, around 2575 Ma and 2500 Ma, respectively (Fig. 14). The activity of  
983 structure S2 seems to have ceased as early as c. 2550 Ma, whereas S3 would have formed  
984 at that time and continued until c. 2450 Ma. S1 records almost continuous hydrothermal  
985 activity between c. 2600 Ma and c. 2450 Ma, for a longer period than HW, WE and  
986 Bonanza, which seem to become static at c. 2500 Ma (Fig. 14). As suggested by Figure  
987 17, multiplying the number of samples and  $^{40}\text{Ar}/^{39}\text{Ar}$  analyses at the Beaufor and Beacon-  
988 2 deposits would have conducted most likely to a similar interpretation regarding their  
989 structural and hydrothermal evolution.  $^{40}\text{Ar}/^{39}\text{Ar}$  ages measured in gold deposits of the  
990 Bourlamaque pluton can be thus attributed to a succession of structurally-driven  
991 hydrothermal events rather than to the passive cooling of the dated minerals. Such  
992 hydrothermal events were obviously not continuous but corresponded to ca. 10-to-20  
993 m.y. pulses of distributed deformation and related fluid circulation.

994 The hydrothermal and deformational evolution depicted by Figure 18 is not  
995 obviously limited to the Bourlamaque pluton and there has been probably a similar  
996 succession of hydrothermal events in other auriferous quartz-carbonate-tourmaline vein  
997 systems of the Val d'Or mining district. If correct, this means that these orogenic gold  
998 deposits were formed much later than usually proposed in literature and for a time length  
999 of more than 150 m.y., during the incremental deformation of alternating, seismically  
1000 active segments of crustal faults systems along which episodic flow is associated with  
1001 fluid pressure cycling and episodic fluid redistribution. Such a duration of crustal faulting  
1002 appears to be much longer than documented in modern crustal-scale fault settings such as  
1003 the San Andreas and the North-Anatolian fault zones along which deformation proceeds  
1004 since up to 40 m.y, which is, however, a minimum value since deformation and faulting  
1005 are still active today. Such a long duration of crustal faulting in the Abitibi Greenstone  
1006 Belt, can be tentatively attributed to the geodynamic context of the Archean, with higher  
1007 geothermal gradients and weak lithospheres in which competent layers are limited to a  
1008 thin brittle crust that favour distributed strains, as documented in a number of  
1009 Precambrian terranes (e.g. Choukroune et al., 1995; Chardon et al., 2008; Cagnard et al.,  
1010 2007; Gapais et al., 2009), as well as by analogue and numerical modeling in which  
1011 horizontal flow of the lower ductile crust combines with distributed shortening of the  
1012 upper brittle crust (e.g. Cagnard et al., 2006; Cruden et al., 2006; Rey and Houseman,  
1013 2006; Gray and Pysklywec, 2010). As a consequence, Precambrian belts tend to show  
1014 much slower cooling rates than modern ones (e.g. Willigers et al., 2002), and long-lasting  
1015 magmatic and deformation histories of the order of 100 Ma or more with rather steady  
1016 kinematic frameworks (e.g. Gapais et al., 2005; Chardon and Jayananda, 2008; Taylor et  
1017 al., 2020).

1018

1019 **Declaration of Competing Interest.**

1020 The authors declare that they have no known competing financial interests or  
1021 personal relationships that could have appeared to influence the work reported in this  
1022 paper.

1023

1024 **Acknowledgements**

1025           The Natural Science and Engineering Council of Canada (NSERC) has provided  
 1026 research grants to A. Tremblay (NSERC-PG105669). This contribution is part of Jérémie  
 1027 Lemarchand (JL) PhD thesis at the Université du Québec à Montreal (UQAM). JL  
 1028 benefited of financial support from BMP-Innovation (FQRNT/NSERC) and DIVEX  
 1029 grants. We sincerely thank E.J. Cowan and an anonymous reviewer, as well as the  
 1030 associate editor, O. Kreuzer, for critical comments that improved the manuscript. Thanks  
 1031 to C. Gobeil and D. Vermette of Alexis Minerals Inc. for help and support for field work  
 1032 in the Lac-Herbin mine and the Val d'Or area. Thanks are also due to M. Laithier, A.  
 1033 Desaulniers and M. Perrot for drawing the figures.

1034

1035 **References**

- 1036 Alexandrov, P., Ruffet, G. and Cheilletz, A., 2002. Muscovite recrystallization and  
 1037 saddle-shaped  $^{40}\text{Ar}/^{39}\text{Ar}$  age spectra: examples from the Blond granite (Massif  
 1038 Central, France). *Geochimica et Cosmochimica Acta* 66: 793–1807.
- 1039 Anglin, C.D., Jonasson, I.R., and Franklin, J.M., 1996. Sm-Nd dating of scheelite and  
 1040 tourmaline; implications for the genesis of Archean gold deposits, Val d'Or,  
 1041 Canada. *Economic Geology* 91: 1372-1382.
- 1042 Bedeaux, P., Pilote, P., Daigneault, R., and Rafini, S., 2017. Synthesis of the structural  
 1043 evolution and associated gold mineralization of the Cadillac Fault, Abitibi,  
 1044 Canada. *Ore Geology Reviews* 82: 49-69.
- 1045 Berryman, K.R., Cochran, U.A., Clark, K.J., Biasi, G.P., Langridge, R.M., and Villamor,  
 1046 P., 2012. Major earthquakes occur regularly on an isolated plate boundary fault. *Science*  
 1047 336: 1690-1693.
- 1048 Boullier, A.-M., Firdaus, K., and Robert, F., 1998. On the significance of aqueous fluid  
 1049 inclusions in gold-bearing quartz vein deposits from the southeastern Abitibi  
 1050 subprovince (Québec, Canada). *Economic Geology* 93: 216-223.
- 1051 Bosse, V., Feraud, G., Ruffet, G., Balleuvre, M., Peucat, J.-J., and De Jong, K., 2000. Late  
 1052 Devonian subduction and early-orogenic exhumation of eclogite-facies rocks  
 1053 from the Champtoceaux Complex (Variscan belt, France). *Geological Journal* 35:  
 1054 297-325.
- 1055 Cagnard, F., Gapais, D. and Barbey, P., 2007. Collision tectonics involving juvenile  
 1056 crust: the example of the southern Svecofennides. *Precambrian Research* 154:  
 1057 125–141.
- 1058 Cagnard, F., Brun, J.P. and Gapais, D., 2006. Modes of thickening of analogue weak  
 1059 lithospheres. *Tectonophysics*, 421: 145–160.

- 1060 Castonguay, S., Ruffet, G., and Tremblay, A. 2007. Dating polyphase deformation across  
 1061 low-grade metamorphic belts: an example based on  $^{40}\text{Ar}/^{39}\text{Ar}$  muscovite age  
 1062 constraints from the southern Quebec Appalachians, Canada. *Geological Society  
 1063 of America Bulletin* 119: 978-992.
- 1064 Castonguay, S., Ruffet, G., Tremblay, A., and Féraud, G., 2001. Tectonometamorphic  
 1065 evolution of the southern Quebec Appalachians:  $^{40}\text{Ar}/^{39}\text{Ar}$  evidence for  
 1066 Ordovician crustal thickening and Silurian exhumation of the internal Humber  
 1067 zone. *Geological Society of America Bulletin* 113: 144–160.
- 1068 Chardon, D. and Jayananda, M., 2008. Three-dimensional field perspective on  
 1069 deformation, flow and growth of the lower continental crust (Dharwar craton,  
 1070 India). *Tectonics*, 27, TC 1014. doi:10.1029/2007TC002120.
- 1071 Chardon, D., Jayananda, M., Chetty, T.R.K. and Peucat, J.-J., 2008. Precambrian  
 1072 continental strain and shear zone patterns: south Indian case. *Journal Geophysical  
 1073 Research* 113, B08402. doi:10.1029/2007JB005299.
- 1074 Cheilletz, A., Ruffet, G., Marignac, C., Kolli, O., Gasquet, D., Féraud, G., and Bouillin,  
 1075 J.P., 1999.  $^{40}\text{Ar}/^{39}\text{Ar}$  dating of shear zones in the Variscan basement of the Greater  
 1076 Kabylia (Algeria). Evidence of an Eo-Alpine event at 128 Ma (Hauterivian–  
 1077 Barremian boundary): geodynamic consequences. *Tectonophysics* 306: 97–116.
- 1078 Choukroune, P., Bouhallier, H. and Arndt, N.T., 1995. Soft lithospheres during periods of  
 1079 Archaean crustal growth or crustal reworking. In: *Early Precambrian Processes*  
 1080 (M.P. Coward and A. Ries, eds). *Geological Society Special Publication* 95: 67–  
 1081 86.
- 1082 Ciborowski, J., Kerr, A., Ernst, R.E., McDonald, I., Minifie, M.J., Harlan, S.S., and  
 1083 Millar, I. 2015. The Early Proterozoic Matachewan Large Igneous Province:  
 1084 Geochemistry, Petrogenesis, and Implications for Earth Evolution. *Journal of  
 1085 Petrology* 56: 1459-1494.
- 1086 Corfu, F. 1993. The evolution of the Southern Abitibi Greenstone Belt in light of precise  
 1087 U-Pb geochronology. *Economic Geology* 88: 1323-1340.
- 1088 Condie, K.C., and Benn, K. 2006. Archean Geodynamics: Similar to or Different from  
 1089 Modern Geodynamics? *American Geophysical Union, Geophysical  
 1090 Monograph* 164, p. 47-59.
- 1091 Connolly, J.A.D. 2010. The mechanics of metamorphic fluid expulsion. *Elements* 6:  
 1092 165-171.
- 1093 Couture, J.-F., Pilote, P., Machado, N., and Desrochers, J.-P., 1994, Timing of gold  
 1094 mineralization in the Val-d'Or camp, southern Abitibi belt: Evidence 2020for two  
 1095 distinct mineralization events. *Economic Geology* 89: 1542–1551.
- 1096 Cowan, E.J. 2020. Deposit-scale structural architecture of the Sigma-Lamaque gold  
 1097 deposit, Canada – insights from a newly proposed 3D method for assessing  
 1098 structural controls from drill hote data. *Mineralium Deposita* 55: 217-240.
- 1099 Cox, S.F. 2005. Coupling between deformation, fluid pressures, and fluid flow in

- 1100 ore-producing hydrothermal systems at depth in the crust. *Economic Geology*  
1101 100th Anniversary Volume, pp. 39–75.
- 1102 Cox, S.F., Knackstedt, M.A., and Braun, J. 2001. Principles of structural control on  
1103 permeability and fluid flow in hydrothermal systems. *Society of Economic*  
1104 *Geologist Review* 14: 1-24.
- 1105 Cox, S.F., Etheridge, M.A., and Wall, V.J. 1987. The role of fluids in syntectonic mass  
1106 transport, and the localization of metamorphic vein-type ore deposits. *Ore*  
1107 *Geology Reviews* 2: 65-86.
- 1108 Cruden, A.R., Nasser, M.H. and Pysklywec, R., 2006. Surface topography and internal  
1109 strain variation in wide hot orogens from three-dimensional analogue and two-  
1110 dimensional numerical vice models; analogue and numerical modelling of crustal-  
1111 scale processes. *Geological Society Special Publication* 253: 79–104.
- 1112 Dahl, P.S., 1996. The effects of composition on retentivity of argon and oxygen in  
1113 hornblende and related amphiboles: a field-tested empirical model. *Geochimica*  
1114 *Cosmochimica Acta* 60 : 3687–3700.
- 1115 Daigneault, R. 1983. Géologie et géochimie du gisement d’or de la mine Lamaque, Val  
1116 d’Or, Québec. Mémoire de maîtrise, École polytechnique de Montréal, Québec,  
1117 Canada.
- 1118 Daigneault, R., 1996. Couloirs de déformation de la sous-Province de l’Abitibi: Ministère  
1119 des Ressources Naturelles du Québec MB 96-33, 115 p.
- 1120 Daigneault, R., Mueller, W., and Chown, E. 2002. Oblique Archean subduction:  
1121 accretion and exhumation of an oceanic arc during dextral transpression, Southern  
1122 Volcanic Zone, Abitibi Subprovince Canada. *Precambrian Research* 115: 261-  
1123 290.
- 1124 Daoudene, Y., Leclerc, F., and Tremblay, A. 2016. Une histoire tectono-métamorphique  
1125 commune et de longue durée pour les sous-provinces d’Abitibi et d’Opatica,  
1126 Province du Supérieur, Québec, Canada. Ministère de l’Énergie et des Ressources  
1127 naturelles, Québec; MB 2016-01, 43 pages.
- 1128 Daoudene, Y., Tremblay, A., Ruffet, G. and Leclerc, F. 2014. Étude structurale et  
1129 métamorphique de la bordure nord-est de la Ceinture de roches vertes de l’Abitibi,  
1130 Québec, Canada : apport de la thermochronologie  $^{40}\text{Ar}/^{39}\text{Ar}$  et implications  
1131 tectoniques. Ministère des Ressources et de la Faune, Québec.
- 1132 Deckart, K., Feraud, G., and Bertrand, H., 1997. Age of Jurassic continental tholeiites of  
1133 French Guyana/Suriname and Guinea: implications to the opening of the Central  
1134 Atlantic Ocean. *Earth and Planetary Science Letters* 150: 205–220.
- 1135 Deino A., Potts, R. 1992. Age-probability spectra for examination of single-crystal  
1136  $^{40}\text{Ar}/^{39}\text{Ar}$  dating results: examples from Olorgesailie, southern Kenya rift.  
1137 *Quaternary International* 13/14: 47-53.
- 1138 De Putter, T. and Ruffet, G., 2020. Supergene manganese ore records 75 Myr-long

- 1139 Campanian to Pleistocene geodynamic evolution and weathering history of the  
 1140 Central African Great Lakes region - Tectonic drives, climate assists. *Gondwana*  
 1141 *Research* 83: 96-117.
- 1142 De Putter, T., Ruffet, G., Yans, J., and Mees, F. 2015. The age of supergene manganese  
 1143 deposits in Katanga and its implications for the Neogen evolution of African  
 1144 Great Lakes Region. *Ore Geology Reviews* 71: 350-362.
- 1145 Dimroth, E., Imreh, L., Goulet, N., and Rocheleau, M., 1983, Evolution of the south-  
 1146 central segment of the Archean Abitibi belt, Quebec. Part II: Tectonic evolution  
 1147 and geomechanical model: *Canadian Journal of Earth Sciences* 20: 1355–1373.
- 1148 Dodson, M.H. 1973. Closure temperature in cooling geochronological and petrological  
 1149 systems. *Contributions to Mineralogy and Petrology* 40: 259-274.
- 1150 Dubé, J. 2018. Caractérisation métallogénique et structurale de la minéralisation aurifère  
 1151 des gisements Triangle et Cheminée No. 4, Val d'Or, Abitibi, Québec. Mémoire  
 1152 de maîtrise, Université du Québec à Chicoutimi, Québec, Canada.
- 1153 Ducharme, Y., Stevenson, R.K. and Machado, N. 1997. Sm-Nd geochemistry and U-Pb  
 1154 geochronology of the Preissac and La Motte leucogranites, Abitibi Subprovince;  
 1155 *Canadian Journal of Earth Sciences* 34: 1059–1071.
- 1156 Dunlap, W.J., 1997. Neocrystallization or cooling?  $^{40}\text{Ar}/^{39}\text{Ar}$  ages of white micas from  
 1157 low-grade mylonites. *Chemical Geology* 143: 181–203.
- 1158 Easton, R.M. 2000. Metamorphism of the Canadian Shield, Ontario, Canada. I. The  
 1159 Superior Province. *The Canadian Mineralogist* 38: 287-317.
- 1160 Faure, S. 2015. Relations entre les minéralisations aurifères et les isogrades  
 1161 métamorphiques en Abitibi. Rapport. Projet CONSOREM 2013-03. 52 p.
- 1162 Feng, R., Kerrich, R., McBride, S. and Farrar, E. 1992.  $^{40}\text{Ar}/^{39}\text{Ar}$  age constraints on the  
 1163 thermal history of the Archean Abitibi greenstone belt and the Pontiac  
 1164 subprovince: implications for terrane collision, differential uplift, and overprinting  
 1165 of gold deposits. *Canadian Journal of Earth Sciences* 29: 1389-1411.
- 1166 Fleck, R.J., Sutter, J.F., and Elliot, D.H., 1977. Interpretation of discordant  $^{40}\text{Ar}/^{39}\text{Ar}$  age  
 1167 spectra of Mesozoic tholeiites from Antarctica. *Geochimica Cosmochimica Acta*  
 1168 41 : 15-32.
- 1169 Fontaine, A., Dubé, B., Malo, M., Doucet, D. 2018. Geology of the Chechoo gold  
 1170 property, Eeyou Istchee Baie-James, Superior Province, northern Quebec.  
 1171 Geological Survey of Canada, Open File 8403, 24 pages.
- 1172 Fontaine, A., Dubé, B., Malo, M., Ravenelle, J.-F., Fournier, E., McNicoll, V., Beausoleil,  
 1173 C., Prud'homme, and N. Goutier, J. 2017. The Éléonore gold mine: exploration,  
 1174 discovery and understanding of an emerging gold district in Eeyou Estchee  
 1175 LJames Bay, Superior Province, northern Québec, Canada. In «Proceedings of  
 1176 Exploration 17: Sixth Decennial International Conference on Mineral Exploration,  
 1177 edited by V. Tschirhart and M.D. Thomas, p. 601-617.

- 1178 Fortier, S. M. and Gilettit B. J., 1989. An empirical model for predicting diffusion  
1179 coefficients in silicate minerals. *Science* 245: 1481 - 1484.
- 1180 Gapais, D., Cagnard, F., Gueydan, F., Barbey, P., and Ballèvre, M. 2009. Mountain  
1181 building and exhumation processes through time: inferences from nature and  
1182 models. *Terra Nova* 21: 188-194.
- 1183 Gapais, D., Potrel, A., Machado, N. and Hallot, E., 2005. Kinematics of long-lasting  
1184 Paleoproterozoic transpression within the Thompson Nickel Belt (Manitoba,  
1185 Canada). *Tectonics* 24,TC3002; doi: 10.1029/2004TC001700.
- 1186 Goldfarb, R.J., Groves, D.I., and Gardoll, S. 2001. Orogenic gold and geologic time: a  
1187 global synthesis. *Ore Geology Reviews* 18: 1-75.
- 1188 Groves, D.I., Goldfarb, R.J., Knox-Robinson, C.M., Ojala, J., Gardoll, S., Yun, G.Y., and  
1189 Holyland, P. 2000. Late-kinematic timing of orogenic gold deposit and significance for  
1190 computer-based exploration techniques with emphasis on the Yilgarn Block,  
1191 Western Australia. *Ore Geology Reviews* 17: 1-38.
- 1192 Groves, D.I., Goldfarb, R.J., Gebre-Mariam, M., Hagemann, S.G., and Robert, F. 1998.  
1193 Orogenic gold deposits: a proposed classification in the context of their crustal  
1194 distribution and relationships to other gold deposit types. *Ore Geology Reviews*  
1195 13: 7-27.
- 1196 Gray, R. and Pysklywec, R.N., 2010. Geodynamic models of Archean continental  
1197 collision and the formation of mantle lithosphere keels. *Geophysical Research*  
1198 *Letters* 37: 1-5.
- 1199 Hames, W. E., Cheney, J. T. and Tracy, R. J., 2008. Single-crystal  $^{40}\text{Ar}/^{39}\text{Ar}$  age variation  
1200 in muscovite of the Gassetts Schist and associated gneiss, Vermont Appalachians.  
1201 *American Mineralogist* 93: 384-395.
- 1202 Hanes, J.A., Archibald, D.A., Hogson, C.J., and Robert, F. 1992. Dating of Archean  
1203 auriferous quartz vein deposits in the Abitibi Greenstone Belt, Canada.  $^{40}\text{Ar}/^{39}\text{Ar}$   
1204 evidence for a 70-100 Ma time gap between plutonism-metamorphism and  
1205 mineralization. *Economic Geology* 87: 1849-1861.
- 1206 Harrison, T.M., Célérier, J., Aikman, A.B., Hermann, J., and Heizler, M.T. 2009.  
1207 Diffusion of  $^{40}\text{Ar}$  in muscovite. *Geochimica Cosmochimica Acta* 73: 1039–1051.
- 1208 Hubert, C., 1990. Geological framework, evolution and structural setting of gold and base  
1209 metal deposits of the Abitibi greenstone belt, Canada. *Univeristy of Western*  
1210 *Australia Short Courses Notes* 24, p. 53–62.
- 1211 Jäger, E., Niggli, E., and Wenk, E., 1967. Rb–Sr Altersbestimmungen an Glimmern der  
1212 Zentralalpen. *Beiträge zur Geologischen Karte der Schweiz, Neue Folge* 134, 67  
1213 pages.
- 1214 Jemielita RA, Davis DW, and Krogh TE. 1990. U-Pb evidence for Abitibi gold  
1215 mineralization postdating greenstone magmatism and metamorphism. *Nature* 346:  
1216 831–834.
- 1217 Jourdan, F., and Renne, P. R. (2007). Age calibration of the Fish Canyon sanidine

- 1218  $^{40}\text{Ar}/^{39}\text{Ar}$  dating standard using primary K–Ar standards. *Geochimica et*  
 1219 *Cosmochimica Acta* 71(2): 387-402.
- 1220 Jourdan, F., Verati, C., and Féraud, G. (2006). Intercalibration of the Hb3gr  $^{40}\text{Ar}/^{39}\text{Ar}$   
 1221 dating standard. *Chemical Geology*, 231(3): 177-189.
- 1222 Kamber, B.S., Blenkinsop, T.G., Villa, I.M., and Dahl, P.S., 1995. Proterozoic  
 1223 transpressive deformation in the Northern Marginal Zone, Limpopo Belt,  
 1224 Zimbabwe. *Journal of Geology* 103: 493–508.
- 1225 Kamineni, D.C., Stone, D., and Peterman, Z.E., 1990. Early Proterozoic deformation in  
 1226 the western Superior Province. *Geological Society of America Bulletin* 102:  
 1227 1623-1634.
- 1228 Kerrich, R. and Cassidy, K.F. 1994. Temporal relationships of lode gold mineralization to  
 1229 accretion, magmatism, metamorphism and deformation - Archean to present – a  
 1230 review. *Ore Geology Review* 9 : 263-310.
- 1231 Krogh, T.E., 1993. High precision U-Pb ages for granulite metamorphism and  
 1232 deformation in the Archean Kapuskasing structural zone, Ontario: implications  
 1233 for structure and development of the lower crust. *Earth and Planetary Science*  
 1234 *Letters* 119: 1-18.
- 1235 Lamb, S. 2011. Cenozoic tectonic evolution of the New Zealand plate-boundary zone : a  
 1236 paleomagnetic perspective. *Tectonophysics* 509, 135-164.
- 1237 Lemarchand, J. 2012. Les minéralisations filoniennes aurifères de pluton de Bourlamaque  
 1238 (Val d’Or, Abitibi) : synthèse structurale et apport de la datation  $^{40}\text{Ar}/^{39}\text{Ar}$ .  
 1239 Ph.D. thesis. Université du Québec à Montréal-Université de Rennes 1.
- 1240 Ludden, J., Hubert, C., and Gariépy, C., 1986, The tectonic evolution of the Abitibi  
 1241 greenstone belt of Canada. *Geological Magazine* 123: 153–166
- 1242 Malo, M., Ruffet, G., Pincivy, A., and Tremblay, A., 2008. A  $^{40}\text{Ar}/^{39}\text{Ar}$  study of oceanic  
 1243 and continental deformation processes during an oblique collision: Taconian  
 1244 orogeny in the Quebec reentrant of the Canadian Appalachian. *Tectonics* 27: 1–  
 1245 29.
- 1246 Moorehead, J., Tremblay, A., Pelz, P., and Beaudoin, G., 1998. Géologie de la mine  
 1247 Louvicourt, in Pilote, P., Moorhead, J., and Mueller, W., eds., Développement  
 1248 d’un arc volcanique, la région de Val-d’Or, Ceinture de l’Abitibi - Volcanologie  
 1249 physique et évolution métallogénique: Association Géologique du Canada Guide  
 1250 d’excursion A-2, p. 39–58.
- 1251 Morasse, S., 1998, Geology, structure and timing of gold mineralization at the Kiena  
 1252 deposit, Val d’Or, Québec: Unpublished Ph.D. thesis, Kingston, ON, Queen’s  
 1253 University.
- 1254 Morfin, S., Sawyer, E.W., and Bandyayera, D. 2013. Large volumes of anatectic melt  
 1255 retained in granulite facies migmatites: an injection complex in northern Quebec.  
 1256 *Lithos* 168-169: 200-218.

- 1257 Mortensen, J.K. and Card, K.D., 1993, U-Pb age constraints for the magmatic and  
1258 tectonic evolution of the Pontiac subprovince. *Canadian Journal of Earth Sciences*  
1259 30: 1970–1980.
- 1260 Neumayr, P., Hagemann, S.G., and Couture, J.-F., 1999, Structural setting, textures, and  
1261 timing of hydrothermal vein systems in the Val d'Or camp, Abitibi, Canada:  
1262 Implications for the evolution of transcrustal, second- and third-order fault zones  
1263 and gold mineralization: *Canadian Journal of Earth Sciences* 37: 95–114.
- 1264 Nuriel, P., Craddock, J., Kylander-Clark, A.R.C., Tonguç Uysal, I., Karabacak, V., Dirik,  
1265 R.K., Harcker, and B.R., Weinberger, R. 2019. Reactivation history of the North  
1266 Anatolian fault zone based on calcite age-strain analyses. *Geology* 47: 465-469.
- 1267 Olivo GR, Isnard H, Williams-Jones AE, and Gariépy C. 2007. Pb isotope compositions  
1268 of pyrite from the C quartz-tourmaline vein of the Siscoe gold deposit, Val d'Or,  
1269 Quebec: constraints on the origin and age of the gold mineralization. *Economic*  
1270 *Geology* 102: 137–146.
- 1271 Olivo, G.R., Chang, F., and Kyser, T.K. 2006. Formation of the auriferous and barren  
1272 North Dipper veins in the Sigma mine, Val d'Or, Canada: Constraints from  
1273 structural, mineralogical, fluid inclusion, and isotopic data. *Economic Geology*  
1274 101: 607 - 631.
- 1275 Passchier, C.W., and Trouw, R.A.J., 1996, *Micro-tectonics*: Berlin Heidelberg, Springer-  
1276 Verlag Editions, 289 p.
- 1277 Percival, J. 2007. *Geology and metallogeny of the Superior Province, Canada*. In W. D.  
1278 Goodfellow (ed). *Mineral Deposits of Canada: A Synthesis of Major Deposit-*  
1279 *Types District Metallogeny, the Evolution of Geological Provinces, and*  
1280 *Exploration Methods*. Geological Association of Canada, Mineral Deposits  
1281 Division, Special Publication, p. 903-928
- 1282 Pitra P., Ballèvre M. and Ruffet G. (2010). Inverted metamorphic field gradient towards a  
1283 Variscan suture zone (Champtoceaux Complex, Armorican Massif, France).  
1284 *Journal of Metamorphic Geology* 28/2, 183-208.
- 1285 Popov, A.A., Sobolev, S.V., and Zoback, M.D. 2012. Modeling evolution of the San  
1286 Andreas Fault system in northern and Central California. *Geochemistry,*  
1287 *Geophysics, Geosystems (G<sup>3</sup>)* 13, doi. 10.1029/2012GC004086.
- 1288 Powell, W.G., Hodgson, C.J., Hanes, J.A., Carmichael, D.M., McBride, S., and Farrar,  
1289 E., 1995, 40Ar-39Ar geochronological evidence for multiple postmetamorphic  
1290 hydrothermal events focused along faults in the southern Abitibi greenstone belt:  
1291 *Canadian Journal of Earth Sciences* 32: 768–786.
- 1292 Renne, P.R., Balco, G., Ludwig, R.L., Mundil, R., and Min, K., 2011. Response to the  
1293 comment by W.H. Schwarz et al. on "Joint determination of <sup>40</sup>K decay constants  
1294 and <sup>40</sup>Ar\*/<sup>40</sup>K for the Fish Canyon sanidine standard, and improved accuracy for  
1295 <sup>40</sup>Ar/<sup>39</sup>Ar geochronology" by PR Renne et al. (2010). *Geochimica et*  
1296 *Cosmochimica Acta*, 75: 5097-5100.

- 1297 Renne, P.R., Mundil, R., Balco, G., Min, K., and Ludwig, R.L., 2010. Joint determination  
 1298 of  $^{40}\text{K}$  decay constants and  $^{40}\text{Ar}^*/^{40}\text{K}$  for the Fish Canyon sanidine standard, and  
 1299 improved accuracy for  $^{40}\text{Ar}/^{39}\text{Ar}$  geochronology. *Geochimica et Cosmochimica*  
 1300 *Acta* 74: 5349–5367.
- 1301 Rey, P. and Houseman, G., 2006. Lithospheric scale gravitational flow: the impact of  
 1302 body forces on orogenic processes from Archaean to Phanerozoic. In: *Analogue*  
 1303 *and Numerical Modelling of Crustal-Scale Processes* (S. Buiter and G. Schreurs,  
 1304 eds). *Geological Society Special Publication*, 253: 153–167.
- 1305 Rezeau, H., Moritz, R., and Beaudoin, G., 2017. Formation of Archean batholith-hosted  
 1306 gold veins at the Lac Herbin deposit, Val d’Or district, Canada: mineralogical and  
 1307 fluid inclusion constraints. *Mineralium Deposita* 52: 421-442. DOI  
 1308 10.1007/s00126-016-0669-5.
- 1309 Robert, F. 2001. Syenite-associated disseminated gold deposits in the Abitibi greenstone  
 1310 belt, Canada. *Mineralium Deposita*, 36(6): 503-516.
- 1311 Robert, F., 1989. Internal structure of the Cadillac tectonic zone, southeast of Val-d’Or,  
 1312 Abitibi greenstone belt, Quebec: *Canadian Journal of Earth Sciences* 26: 2661–  
 1313 2675.
- 1314 Robert, F. 1990, Structural setting and control of gold-bearing quartz veins of the Val-  
 1315 d’Or area, southeastern Abitibi subprovince: *University of Western Australia*  
 1316 *Short Course Notes* 24, p. 167–210.
- 1317 Robert, F. 1994, Vein fields in gold districts: Example of Val-d’Or, southeastern Abitibi  
 1318 subprovince, Québec: *Geological Survey of Canada Paper* 94-1C, p. 295–302.
- 1319 Robert, F., and Brown, A.C. 1986. Archean gold-quartz veins at the Sigma mine, Abitibi  
 1320 Greenstone Belt, Quebec: Part I. Geological relations and formation of the vein  
 1321 system. Part II. Vein paragenesis and hydrothermal alteration. *Economic Geology*  
 1322 81: 578-616.
- 1323 Robert, F., and Kelly, W.C. 1987. Ore-forming fluids in Archean gold-bearing quartz  
 1324 veins at the Sigma mine, Abitibi Greenstone Belt, Quebec, Canada. *Economic*  
 1325 *Geology* 82: 1464-1482.
- 1326 Robert, F., Poulsen, K.H., Cassidy, K.F., and Hodgson, C.J. 2005. Gold metallogeny of  
 1327 the Superior and Yilgarn cratons. *Economic Geology 100th Anniversary Volume*,  
 1328 pp. 1001–1033.
- 1329 Roddick, J. 1983. High precision intercalibration of  $^{40}\text{Ar}$ - $^{39}\text{Ar}$  standards. *Geochimica et*  
 1330 *Cosmochimica Acta*, 47(5): 887-898.
- 1331 Roddick, J.C., Cliff, R. A. and Rex, D. C., 1980. The evolution of excess argon in alpine  
 1332 biotites -  $^{40}\text{Ar}/^{39}\text{Ar}$  analysis: *Earth Planetary Science Letters* 48: 185-208.
- 1333 Roussy, J. 2003. Relations entre la distribution de l’or, la structure, la composition des  
 1334 veines et de l’altération hydrothermale à la mine Beaufor, Val d’Or, Québec.  
 1335 M.Sc. thesis, Laval University, 311 pages.
- 1336 Ruffet, G., Féraud, G., Balèvre, M., and Kiénaast, J.-R., 1995. Plateau ages and excess

- 1337 argon in phengites: an  $^{40}\text{Ar}$ – $^{39}\text{Ar}$  laser probe study of Alpine micas (Sesia Zone,  
1338 Western Alps, northern Italy). *Chemical Geology* 121: 327–343.
- 1339 Ruffet, G., Féraud, G., and Amouric, M., 1991. Comparison of  $^{40}\text{Ar}$ – $^{39}\text{Ar}$  conventional  
1340 and laser dating of biotites from the North Trégor Batholith. *Geochimica and*  
1341 *Cosmochimica Acta* 55: 1675–1688.
- 1342 Ruffet, G., Gruau, G., Ballèvre, M., Féraud, G., and Philippot, P. 1997. Rb/Sr and  
1343  $^{40}\text{Ar}/^{39}\text{Ar}$  laser probe dating of high-pressure phengites from the Sesia zone  
1344 (Western Alps): underscoring of excess argon and new age constraints on the  
1345 high-pressure metamorphism. *Chemical Geology* 141: 1-18.
- 1346 Sauvé, P., Imreh, L., and Trudel, P., 1993. Description des gîtes d'or de la région de Val-  
1347 d'Or: Ministère des Ressources Naturelles du Québec MM 91-03, 178 p.
- 1348 Sasseville, C., and Jebrak, M. 2017. Gold epichrons in the Abitibi greenstone belt,  
1349 Canada, and the impact of early Proterozoic Matachewan LIP event.
- 1350 Sawyer, E.W., and Benn, K. 1993. Structure of the high-grade Opatca Belt and the  
1351 adjacent low-grade Abitibi Subprovince, Canada: an Archean mountain front.  
1352 *Journal of Structural Geology* 15: 1443-1458.
- 1353 Scharer, K., Weldon II, R., Streig, A., and Fumal, T. 2014. Paleoearthquakes at Frazier  
1354 Mountain, California delimit extent and frequency of pas San Andreas Fault  
1355 ruptures along 1857 trace. *Geophysical Research Letters* 41: 4527-4534.
- 1356 Scott, C.R., Mueller, W.U., and Pilote, P. 2002. Physical volcanology, stratigraphy, and  
1357 litho-geochemistry of an Archean volcanic arc: evolution from plume-related  
1358 volcanism to arc rifting of SE Abitibi Greenstone Belt, Val-d'Or, Canada.  
1359 *Precambrian Research* 115: 223-260.
- 1360 Sheldon, H.A., and Ord, A. 2005. Evolution of porosity, permeability and fluid pressure  
1361 in dilatant faults post-failure: implications for fluid flow and mineralization.  
1362 *Geofluids* 5: 272-288.
- 1363 Sibson, R.H., 2001. Seismogenic framework for hydrothermal transport and ore  
1364 deposition. *Reviews in Economic Geology* 14: 25-50.
- 1365 Sibson, R.H., Robert, F., and Poulsen, K.H., 1988, High-angle reverse faults, fluid-  
1366 pressure cycling, and mesothermal gold-bearing quartz deposits: *Geology* 16:  
1367 551–555.
- 1368 Sizova, E., Gerya, T., Brown, M., and Perchuk, L.L. 2010. Subduction styles in the  
1369 Precambrian: Insight from numerical experiments. *Lithos* 116: 209-229.
- 1370 Stuwe, K. 1998. Tectonic constraints on the timing relationships of metamorphism, fluid  
1371 production and gold-bearing quartz vein emplacement. *Ore Geology Reviews* 13:  
1372 219-228.
- 1373 Taner, M. F., and Trudel, P. 1989. Bourlamaque batholith and it's gold potential, Val  
1374 d'Or, Québec. *CIM Bulletin* 82: 33-42.
- 1375 Tartese, R. and Boulvais, P., 2010. Differentiation of peraluminous leucogranites “en  
1376 route” to the surface. *Lithos* 114: 353-368.

- 1377 Tartese, R., Ruffet, G., Poujol, M., Boulvais, P., and Ireland, T. R. 2011. Simultaneous  
1378 resetting of the muscovite K-Ar and monazite U-Pb geochronometers: A story of  
1379 fluids. *Terra Nova* 23: 390–398.
- 1380 Taylor, R.J.M., Johnson, T.E., Clark, C., and Harrison, R.J. 2020. Persistence of melt-  
1381 bearing Archean lower crust for >200 m.y. – an example from the Lewisian  
1382 Complex, northwest Scotland. *Geology* 48: 221-225.
- 1383 Tessier, A.C., 1990, Structural evolution and host rock dilation during emplacement of  
1384 gold- bearing quartz veins at Perron deposit, Val-d’Or, Quebec: Unpublished  
1385 M.S. thesis, Kingston, ON, Queen’s University, 242 p.
- 1386 Tremblay, A. 2001. Post-mineralization faults in the Beaufor gold deposit, Abitibi  
1387 Greenstone Belt, Canada: geometry, origin and tectonic implications for the Val  
1388 d’Or mining district. *Economic Geology* 96: 509-524.
- 1389 Tremblay, A., Ruffet, G. and Bédard, J.H. 2011. Obduction of Tethyan-type ophiolites –  
1390 a case-study from the Thetford-Mines ophiolitic Complex, Québec Appalachians,  
1391 Canada. *Lithos* 125: 10-26.
- 1392 Tremblay, A., Daoudene, Y., Ruffet, G. and Leclerc, F. 2019. The Abitibi-Opatca  
1393 contacts, Archean Superior Province (Quebec) – is it a tectonic plate boundary  
1394 suture? GAC-MAC meeting, Québec city, Canada.
- 1395 Turner, G., Huneke, J.C., Podose, F.A., and Wasserbrug, G.J., 1971.  $^{40}\text{Ar}/^{39}\text{Ar}$  ages and  
1396 cosmic ray exposure ages of Apollo 14 samples. *Earth and Planetary Science*  
1397 *Letters* 12: 19–35.
- 1398 Villa, I.M. 2010. Disequilibrium textures versus equilibrium modelling: geochronology at  
1399 the crossroads; in Spalla, M. I., Marotta, A. M. & Gosso, G. (eds) *Advances in*  
1400 *Interpretation of Geological Processes: Refinement of Multi-scale Data and*  
1401 *Integration in Numerical Modelling*. Geological Society, London, Special  
1402 *Publications* 332, 1–15.
- 1403 Villa, I.M., 1998. Isotopic closure. *Terra Nova* 10 : 42–47.
- 1404 West, D.P., Jr., and Lux, D.R., 1993. Direct dating of mylonitization by the  $^{40}\text{Ar}/^{39}\text{Ar}$   
1405 method: An example from the Norumbega fault zone, Maine: *Earth and Planetary*  
1406 *Science Letters* 120: 221-237.
- 1407 Williamson, K., 2001. Analyse structurale des zones aurifères et chronologie des  
1408 événements géologiques à la mine Beacon-2. Laval Université (Quebec), M.Sc.  
1409 thesis, 111 pages.
- 1410 Willigers, J.A., van Gool, J.A.M., Wijbrans, J.R., Krogstad, E.J., and Mezger, K. 2002.  
1411 Posttectonic cooling of the Nagssugtoqidian Orogen and a comparison of  
1412 contrasting cooling histories in Precambrian and Phanerozoic orogens. *The*  
1413 *Journal of Geology* 110: 503-517.
- 1414 Wilkinson, L., Cruden, A.R., and Krogh, T.E. 1999. Timing and kinematics of post-  
1415 Temiskaming deformation within the Larder Lake-Cadillac deformation zone,

- 1416 southwest Abitibi greenstone belt, Ontario, Canada. *Canadian Journal of Earth*  
 1417 *Science* 36: 627-647.
- 1418 Wong, L., Davis, D.W., Krogh, T.E., and Robert, F., 1991, U-Pb zircon and rutile  
 1419 geochronology of Archean greenstone formation and gold mineralization in the  
 1420 Val-d'Or region, Quebec: *Earth and Planetary Science Letters* 104: 325–336.
- 1421 Zweng, P.L., Mortensen, J.K., and Dalrymple, G.B. 1993. Thermochronology of the  
 1422 Camflo gold deposit, Malartic, Quebec: implications for magmatic underplating  
 1423 and the formation of gold-bearing quartz veins. *Economic Geology* 88: 1700-  
 1424 1721.

1425

### 1426 **Figure captions**

- 1427 Figure 1. Diagram  $P_f$ - $\epsilon$ - $t$ . Diagram illustrating the concept of incremental deformation  
 1428 within the fault-valve model of Sibson et al. (1988), and the relationships between  
 1429 fluid pressure ( $P_f$ ) and strain rate ( $\epsilon$ ) fluctuations with time ( $t$ ).
- 1430 Figure 2. Simplified geological map of the southern Abitibi Greenstone Belt (Abitibi  
 1431 supprovince) and adjacent Pontiac subprovince. BP, Bourlamaque pluton; LP,  
 1432 Lacorne pluton; PP, Preissac pluton; LMP, La Motte pluton; FP, Flavrian pluton;  
 1433 LLCfz, Larder Lake-Cadillac fault zone; DPMfz, Destor-Porcupine-Manneville  
 1434 fault zone. Modified from Bedeaux et al. (2017).
- 1435 Figure 3. Geological map of the Val d'Or area and location of the principal vein-type  
 1436 orogenic gold deposits (black dots) of the Val d'Or mining district. See Figure 1  
 1437 for location.
- 1438 Figure 4. Cross-section of the Lac-Herbin gold deposit showing the location of the  
 1439 principal mineralized and barren shear zones. Red, main mineralized shear zones;  
 1440 Yellow, subsidiary mineralized shear zones, Black, barren shear zone. Modified  
 1441 from Lemarchand (2012).
- 1442 Figure 5. Synthetic North-South profiles of mineralized shear zones (red) and  
 1443 crosscutting brittle faults (green) for the Lac-Herbin (a), Beaufor (b) and Beacon-  
 1444 2 (c) mines. Note that almost all the mineralized shear zones shown in red also  
 1445 correspond to mined stopes at each deposit. Modified from Lemarchand (2012).
- 1446 Figure 6. Single-grain  $^{39}\text{Ar}/^{40}\text{Ar}$  results for amphiboles for the Lac-Herbin mine. (a)  
 1447 Density probability diagrams (frequency diagram) of apparent ages and validated  
 1448 ages (plateau and pseudo-plateau – see text for explanation). (b) Validated ages  
 1449 (plateau and pseudo-plateau – see text for explanations) versus depth. (c), (d), (e),  
 1450 (f), (g), (h) and (i) Amphibole  $^{40}\text{Ar}/^{39}\text{Ar}$  age spectra. Apparent age error bars are  
 1451 at the  $1\sigma$  level; errors in the J-parameter are not included. Plateau and pseudo-  
 1452 plateau ages ( $1\sigma$  uncertainties including errors in the J-parameter) are given when  
 1453 applicable. See text for explanations. (J) Mean values of the significant segments  
 1454 of the  $^{37}\text{Ar}_{\text{Ca}}/^{39}\text{Ar}_{\text{K}}$  (# Ca/K) spectra versus depth. See section 5.1 for  
 1455 explanations.
- 1456 Figure 7: Analysed white micas from the HW zone of the Lac-Herbin mine (see Fig. 4 for

- 1457 location) with conventional age spectra (apparent ages vs.  $\%^{39}\text{Ar}_K$ ),  $^{40}\text{Ar}^*$   
 1458 degassing spectra ( $(^{40}\text{Ar}/\Delta\text{VT}^\circ)/(^{40}\text{Ar}/\Delta\text{VT}^\circ)_{\text{Max}}$  vs.  $\%^{39}\text{Ar}_K$ ), weighted age  
 1459 spectra (apparent ages vs.  $\%((^{39}\text{Ar}_K/\Delta\text{VT}^\circ)/(^{39}\text{Ar}_K/\Delta\text{VT}^\circ)_{\text{Max}})$  and resized age  
 1460 spectra (steps of 4% of  $^{39}\text{Ar}_K$  released). See text for explanations. Plateau and  
 1461 pseudo-plateau ages ( $1\sigma$  uncertainties including errors in the J-parameter) are  
 1462 given when applicable. Also shown is the frequency diagram of apparent ages of  
 1463 resized age spectra (see text for explanation).  $\text{VT}^\circ$ , the laser power control  
 1464 voltage, is a proxy indicator of temperature.
- 1465 Figure 8. Analysed white micas from the S2 zone of the Lac-Herbin mine. See caption of  
 1466 Figure 7 and section 5.2.2 for explanations.
- 1467 Figure 9. Analysed white micas from the S1 zone of the Lac-Herbin mine. See caption of  
 1468 Figure 7 and section 5.2.2 for explanations.
- 1469 Figure 10. Analysed white micas from the S3 zone of the Lac-Herbin mine. See caption  
 1470 of Figure 7 and section 5.2.2 for explanations.
- 1471 Figure 11. Analysed white micas from the WE zone of the Lac-Herbin mine. See caption  
 1472 of Figure 7 and section 5.2.2 for explanations.
- 1473 Figure 12. Analysed white micas from the HW3 zone of the Lac-Herbin mine. See  
 1474 caption of Figure 7 and section 5.2.2 for explanations.
- 1475 Figure 13. Analysed white micas from surface samples of the Lac-Herbin mine. See  
 1476 caption of Figure 7 and section 5.2.2 for explanations.
- 1477 Figure 14. Synthesis of the validated ages of Lac-Herbin mine (plateau and pseudo-  
 1478 plateau) obtained on white micas from quartz veins (circles) and shears (squares),  
 1479 grouped by zones (HW, S1, S2, S3, WE, HW3, Bonanza, Flat and surface)  
 1480 superimposed on the probability density diagram of the resized apparent ages. See  
 1481 text for explanation. The red arrows show the sequences of successive  
 1482 components identified during the analysis of the same white mica. White circles  
 1483 or squares represent unvalidated ages.
- 1484 Figure 15. Analysed white micas from the Beaufor mine. See captions of Figure 7 and  
 1485 14, and section 5.2.2 for explanations.
- 1486 Figure 16. Analysed white micas from the Beacon 2 mine. See captions of Figure 7 and  
 1487 14, and section 5.2.2 for explanations.
- 1488 Figure 17. Synthesis of the validated ages (plateau and pseudo-plateau) of the  
 1489 Bourlamaque pluton obtained on amphiboles (triangles) and on white micas  
 1490 (quartz veins as circles and shears as squares) versus depth, superimposed on the  
 1491 probability density diagram of apparent ages. White circles or squares represent  
 1492 unvalidated ages.
- 1493 Figure 18. Synthetic diagram showing the distribution of amphibole and white mica  $^{39}\text{Ar}$ -  
 1494  $^{40}\text{Ar}$  ages obtained during this study, and compilation of the time range of U-Pb  
 1495 and  $^{40}\text{Ar}/^{39}\text{Ar}$  ages measured on different lithologies and for metamorphism in the  
 1496 Val d'Or area, including geochronological data for different gold mines and  
 1497 mining districts of the southern Abitibi Belt (extracted from Powell et al., 1995).  
 1498 Each black line represents a single plateau or sub-plateau  $^{40}\text{Ar}/^{39}\text{Ar}$  age (including  
 1499 the error range) measured during this study; green for amphiboles and yellow for  
 1500 white micas.
- 1501 Genetic links between peak metamorphism and vein-type Au mineralization are debate.

- 1502  $^{40}\text{Ar}/^{39}\text{Ar}$  data indicate long-lasting and sequential hydrothermal activity.
- 1503 Au-rich fluids circulation started around 2650 Ma in the Bourlamaque pluton.
- 1504 Hydrothermal pulses continued for more than 150 m.y., possibly down to c. 2450 Ma.
- 1505
- 1506

Journal Pre-proofs